ARTICLE

Lithium titanate hydrates with superfast and stable cycling in lithium ion batteries

Shitong Wang[1,2], Wei Quan[1], Zhi Zhu[2], Yong Yang[3], Qi Liu[4], Yang Ren[4], Xiaoyi Zhang[4], Rui Xu[5], Ye Hong[1], Zhongtai Zhang[1], Khalil Amine[5], Zilong Tang[1], Jun Lu [5] & Ju Li [2,6]

Lithium titanate and titanium dioxide are two best-known high-performance electrodes that can cycle around 10,000 times in aprotic lithium ion electrolytes. Here we show there exists more lithium titanate hydrates with superfast and stable cycling. That is, water promotes structural diversity and nanostructuring of compounds, but does not necessarily degrade electrochemical cycling stability or performance in aprotic electrolytes. As a lithium ion battery anode, our multi-phase lithium titanate hydrates show a specific capacity of about 130 mA h g^{-1} at ~35 C (fully charged within ~100 s) and sustain more than 10,000 cycles with capacity fade of only 0.001% per cycle. In situ synchrotron diffraction reveals no 2-phase transformations, but a single solid-solution behavior during battery cycling. So instead of just a nanostructured intermediate to be calcined, lithium titanate hydrates can be the desirable final destination.

[1] State Key Lab of New Ceramics and Fine Processing, School of Materials Science and Engineering, Tsinghua University, Beijing 100084, China. [2] Department of Nuclear Science and Engineering, Massachusetts Institute of Technology, Cambridge, Massachusetts 02139, USA. [3] Department of Chemistry, Tsinghua University, Beijing 100084, China. [4] X-ray Science Division, Advanced Photon Source, Argonne National Laboratory, Lemont, Illinois 60439, USA. [5] Chemical Sciences and Engineering Division, Argonne National Laboratory, Lemont, Illinois 60439, USA. [6] Department of Materials Science and Engineering, Massachusetts Institute of Technology, Cambridge, Massachusetts 02139, USA. Correspondence and requests for materials should be addressed to Z.T. (email: tzl@tsinghua.edu.cn) or to J.L. (email: junlu@anl.gov) or to J.L. (email: liju@mit.edu)

Fast-charging electronic devices have experienced dramatic development recently[1]. Compounds on the binary Li_2O–TiO_2 composition line, such as $Li_4Ti_5O_{12}$ ($2Li_2O•5TiO_2$, LTO) and various TiO_2 polymorphs (TO), are generally considered the most promising anode materials for Li-ion batteries in terms of rate capability and cycling stability, as well as the improved safety over graphite anode[2–6]. Producing nanostructured materials on the Li_2O–TiO_2 composition line often requires water-based synthesis such as hydrothermal or sol-gel approaches, and thus one often deals with reaction intermediates that contain water (lithium titanate hydrates, LTHs) in the Li_2O–TiO_2–H_2O ternary composition space (Fig. 1). Because water is considered "harmful" in high-voltage window aprotic electrolytes (free water can be highly reactive to $LiPF_6$, lithium metal anode and lithium alkyl carbonates)[7], most researchers calcine the nanostructured LTHs to completely remove all water by raising temperature to above 500 °C[8]. However, this can cause an unwanted side effect of coarsening and aggregation of the structure. Herein, we demonstrate that the high-temperature calcining may not be necessary. One may only need to remove the more loosely bound water (such as adsorbed and crystallographic water) by heating to a much lower temperature of <260 °C, which does not induce significant coarsening of the nanostructure. The deeply trapped water inside LTHs, or pseudohydrates (i.e., hydroxide or hydroxonium ions or as –OH and –H groups)[9, 10], does not necessarily degrade stability or performance in aprotic electrolytes, even with H_2O:TiO_2 molar ratio as high as 0.41. Indeed, the trapped water can promote structural diversity and nanostructuring that could be highly beneficial for battery performance in aprotic electrolytes.

In this paper, a series of novel materials in the Li_2O–TiO_2–H_2O ternary composition space are discovered via an optimized dehydration induced nanostructuring (ODIN) approach, which is illustrated in Fig. 2 with an accompanying animation (Supplementary Movie 2). They show better electrochemical performances compared to all the Li_2O–TiO_2 materials reported so far (see the comparison in Supplementary Table 1), including

those after nanostructuring, doping and/or coating. As lithium ion battery anode, our novel lithium titanate hydrates can still show a specific capacity of about 130 mA h g^{-1} at ~35 C (fully charged within ~100 s) and sustain more than 10,000 cycles with capacity fade of only 0.001% per cycle. This discovery indicates that the level of dehydration after hydrothermal or sol-gel synthesis should be carefully optimized, since phase transformation driven by dehydration could be a valuable tool for creating composites with nanostructure refinement, and mixed battery and pseudocapacitor features[11], whereas complete dehydration by further heating can coarsen the structures and actually degrade electrochemical performances.

Results

Synthesis and characterization of lithium titanate hydrates. Two-dimensional (2D) crystals may provide kinetic advantage due to plenty of fast Li$^+$ conducting pathways[12]. We set out with layered hydrogen trititanates with a formula of $H_2Ti_nO_{2n+1}•H_2O$ (or $Na_xH_{2-x}Ti_nO_{2n+1}•H_2O$, $2 \leq n \leq 9$, $0 \leq x \leq 2$, due to the incomplete ionic exchange reaction), such as $H_2Ti_2O_5•H_2O$ ($2H_2O•2TiO_2$) and $H_2Ti_3O_7$ ($H_2O•3TiO_2$), which are well known to form nanotubes and nanosheets[8] but unable to support long-life electrochemical cycling in aprotic electrolyte. We then produced a 2D $Li_{1.81}H_{0.19}Ti_2O_5•2H_2O$ precursor (hereafter referred to as LTHs-precursor) by hydrothermal lithiation of layered hydrogen trititanates in LiOH solution[13], which preserves the layered nature with interlayer spacing of 0.8 nm (Supplementary Fig. 1). We then systematically study their performance in electrochemical cycling, as we gradually dehydrate the material (see the *arrow* direction in Fig. 1 and Supplementary Movie 1) by raising the heating temperature. TG (DSC) curves (Fig. 3a and Supplementary Fig. 2) and ex situ XRD patterns (Fig. 3b) reveal that the sample underwent three different stages in the ODIN process. The first weight loss region was 50–130 °C, which corresponded to the loss of absorbed water, and the second region was 130–190 °C, which was mainly attributed to the loss of crystallographic water, with LTHs-precursor
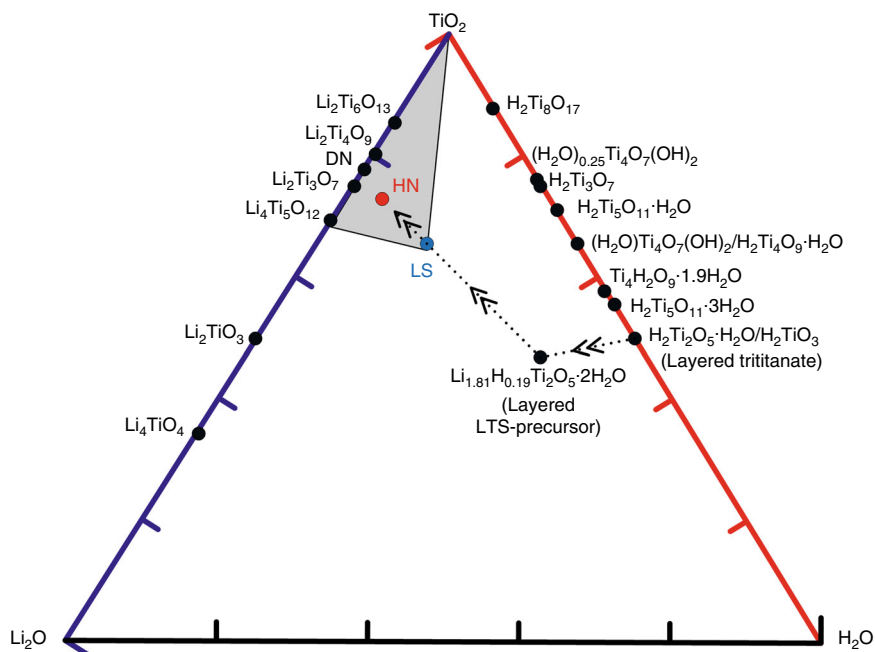

Fig. 1 Calculated ternary phase diagram of Li_2O–TiO_2–H_2O ternary composition space. The *arrow* demonstrates the ODIN process, the *black dot* shows the common phase in the Li_2O–TiO_2–H_2O ternary composition space; and the *blue dot* is the new phase LS; the *shadow* region illustrate the new mixed phase HN composed of $Li_4Ti_5O_{12}$–TiO_2–LS. See also Supplementary Movie 1
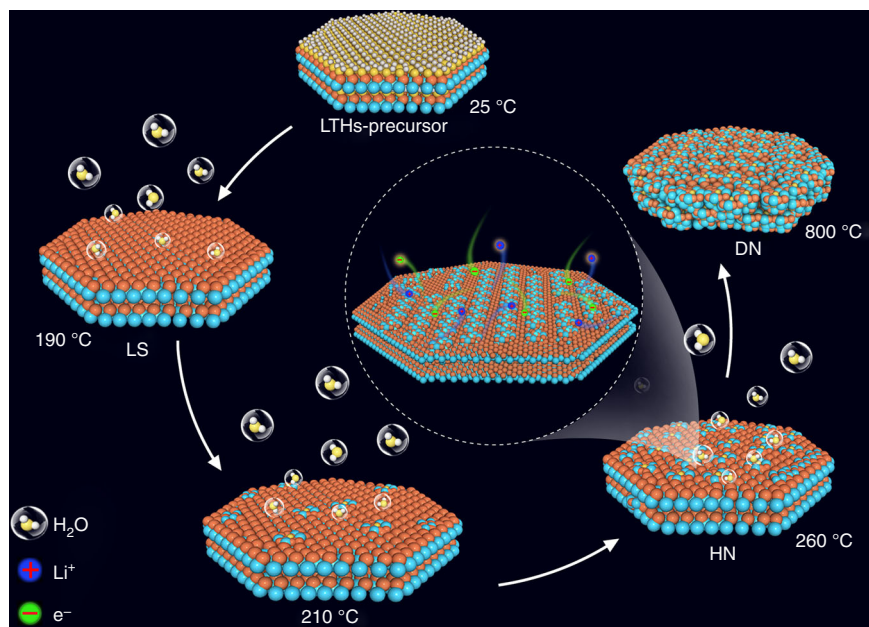
Fig. 2 Schematic diagram in the dehydration process and the fast lithium insertion/extraction within the hydrated nanocomposite (HN) material in battery. The tiny clusters appeared on the nanosheet after 190 °C represent LTO and TO nanocrystallites, and the clusters grow gradually to bigger crystals with the increase of temperature

transforming into a new layered structure, hereon called LS. In situ high-energy X-ray diffraction (HEXRD, Fig. 3c) technique illustrated the transformation of the layered structure. During the thermal ramping, the reflection of layered structure (200) for LTHs-precursor maintained until ~180 °C, and then shifted to a higher 2θ angle at above 190 °C, leading to the decrease of interlayer spacing to 0.6 nm (Supplementary Fig. 3). Fourier transform infrared spectroscopy (FTIR) demonstrates that the main state of proton in LS is hydrogen-bonded Ti–OH (Supplementary Fig. 4). A possible chemical formula of LS is $Li_{1.25}H_{1.63}Ti_2O_{5.44-\sigma}$ (σ represents the O vacancy), based on inductively coupled plasma mass spectroscopy (ICP-MS) and elemental analyzer measurements. Prior to the formation of LS (before dehydrating to 190 °C), the electrochemical performance of dehydrated LTHs-precursor is not satisfactory, because the "free water" can be driven out of the material during electrochemical cycling and therefore severely degrade the aprotic electrochemical system (Supplementary Fig. 5) as previously understood[7].

The last weight loss region was 190–400 °C, which corresponded to the gradual collapse of the layered structure and the growth of three-dimensional (3D) LTO and TO nanocrystallites via a topotactic transformation reaction[14, 15]. With rising temperature in this regime, an increasing proportion of $Li_4Ti_5O_{12}$ and anatase TiO_2 nanocrystallites was obtained (as shown in the *yellow* region and *green* region in Fig. 3b, respectively); correspondingly, the proportion of LS decreased (as shown in the *purple* region in Fig. 3b), and the material became more defective due to loss of water in the 2D lattice. Notably, the peak corresponding to the interlayer spacing of LS disappeared above 350 °C[8], implying the collapse of layered structure. As the temperature reached 400 °C, the diffraction peaks of $Li_4Ti_5O_{12}$ and TiO_2 became steep, indicating growth of 3D crystals. To make our point of pseudohydrates being benign for room-temperature (RT) electrochemical performance, we pick a final dehydration temperature of 260 °C, where a nanocomposite material consisting of defective LS, spinel $Li_4Ti_5O_{12}$ (JCPDS No. 49-0207) and anatase TiO_2 (JCPDS

No. 89-4921) nanocrystallites was obtained, with the individual sets of planes indexed (Supplementary Fig. 6). We call this material the hydrated nanocomposite (HN) state, which still contains significant amount of water in its defected LS component to keep the layered structure, albeit less than LS as illustrated in Fig. 1. The chemical formula of HN is $Li_{1.39}H_{1.18}Ti_2O_{5.29-\sigma}$ (σ represents the O vacancy) based on the same measurements for LS. It is important to note that the hydrogen atoms are distributed homogeneously throughout the bulk of the nanosheets from time-of-flight secondary ion mass spectrometry (TOF-SIMS) depth profile (Supplementary Fig. 7), distinct from surface hydrogenation[16].

Beyond 400 °C, no more water came out. The final product at 800 °C is $Li_4Ti_5O_{12}$ and rutile TiO_2 (JCPDS No. 21-1276), as anatase TiO_2 transformed to rutile TiO_2 at a relatively high temperature of 800 °C. This completely water-free $Li_4Ti_5O_{12}$-TiO_2 nanocomposite (hereafter referred to as DN, dry nanocomposite) is also measured for RT electrochemical performances for comparison. Note that DN (which is the route most researchers took to obtain electrodes on Li_2O–TiO_2 composition axis after hydrothermal synthesis) has coarser structures than HN, due to coarsening and aggregation at higher temperatures (Supplementary Figs. 8, 10). The specific surface area decrease caused by the coarsening is also characterized by N_2 adsorption/desorption (Supplementary Fig. 11). This tradeoff between "water removal" and "nanostructure coarsening" and its impact on electrochemical performance is at the heart of the current work. We will show that removing all water is often an overkill. Instead, the as-synthesized LS and HN through ODIN give the best results.

Electrochemical behavior of lithium titanate hydrates. Electrochemical performance of hydrated LS and HN materials were evaluated and compared to water-free DN. Figure 3d provides the galvanostatic discharge/charge curves of HN, LS and DN at a current density of 100 mA g^{-1} between 1.0 and 2.5 V. LS has a discharge capacity of 174 mA h g^{-1} and the nearly constant
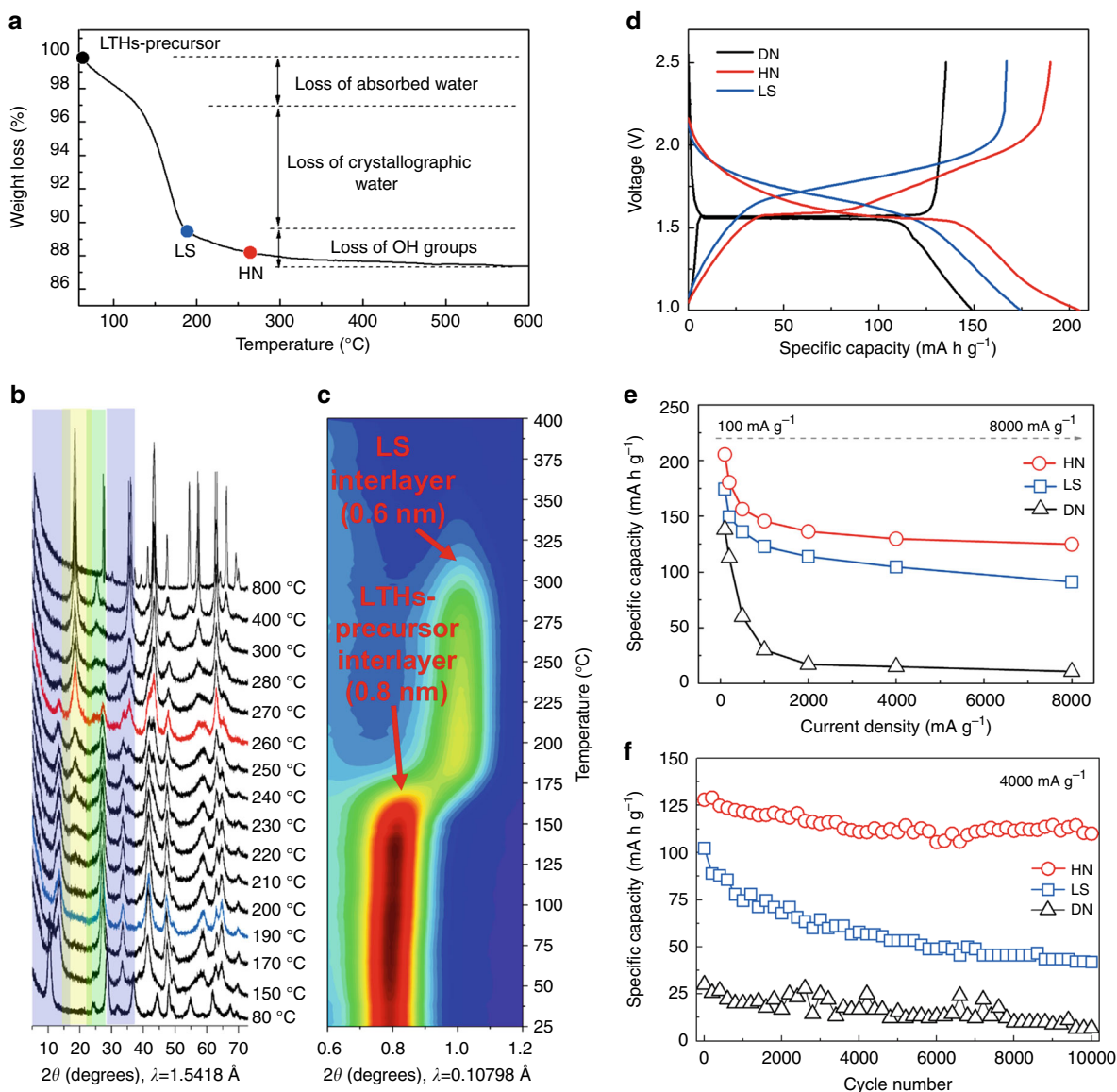
Fig. 3 Characterization of as synthesized materials in the Li_2O–TiO_2–H_2O ternary space. **a** TG analysis; **b** Ex situ XRD patterns and (**c**) contour plot of in situ HEXRD profile (*red* represents a high intensity and *blue* represents a low intensity) of LTHs-precursor heated to different temperatures. Comparison among LS, HN and DN electrode materials in the following three cases: **d** Charge–discharge profiles at 100 mA g^{-1} between 1.0 and 2.5 V (vs Li/Li$^+$); **e** Rate capabilities at different current densities from 200 to 8000 mA g^{-1} and **f** cycling stability at 4000 mA g^{-1}. All RT electrochemical measurements **d–f** were carried out in two-electrode 2032 coin-type half-cells

slope of current-potential curve indicates a quasi-solid-solution behavior. On the other hand, DN reveals a typical battery type of discharge curve with a well-defined voltage plateau and delivers 149 mA h g^{-1} discharge capacity. HN, with a discharge storage behavior combining the features of the following three: sloping current-potential for LS, nanosized LTO and TO[17, 18], as well as the additional Li storage at the interfaces, exhibiting high capacity of 205 mA h g^{-1}. Cyclic voltammetry (CV) curves for LS, HN and DN materials further demonstrate the composite nature of HN electrode (Supplementary Fig. 12).

The rate capability of the three materials is shown in Fig. 3e. When discharged at 100 mA g^{-1}, owing to the surface reactions of LS together with the additional Li storage at the interfaces among $Li_4Ti_5O_{12}$-TiO_2-LS, HN delivers a reversible capacity of 205 mA h g^{-1}, which is higher than LS (174 mA h g^{-1}) or DN (138 mA h g^{-1}). As the current density increases to 8000 mA g^{-1}, the capacity of HN and LS gently decrease to 124 mA h g^{-1} and

91 mA h g^{-1}, respectively, which demonstrate their superior rate capabilities. The capacity of DN, in contrast, plummets to 17 mA h g^{-1} at 2000 mA g^{-1} and ends in almost zero at higher current density. As a result, LS demonstrates a quite stable performance for ultrafast lithium ions insertion/extraction at a high current rate of 8000 mA g^{-1} (~70 C) for 1000 cycles with 76% capacity retention of its initial capacity 106 mA h g^{-1} (Supplementary Fig. 13). The HN electrode exhibits superior cycling capacity of about 130 mA h g^{-1} at 4000 mA g^{-1} (fully charged within ~100 s) and sustains >10,000 cycles with 86% capacity retention (Fig. 3f). Moreover, nearly complete nanosheet morphology of HN was retained after 10,000 ultrafast cycling under transmission electron microscopy (TEM; Supplementary Fig. 14) observation. From X-ray photoelectron spectroscopy (XPS) analysis of the electrodes after cycling (Supplementary Fig. 15), we know that Li_2CO_3 and ROCOOLi species are the major components on the surface of LS and HN electrodes, due to
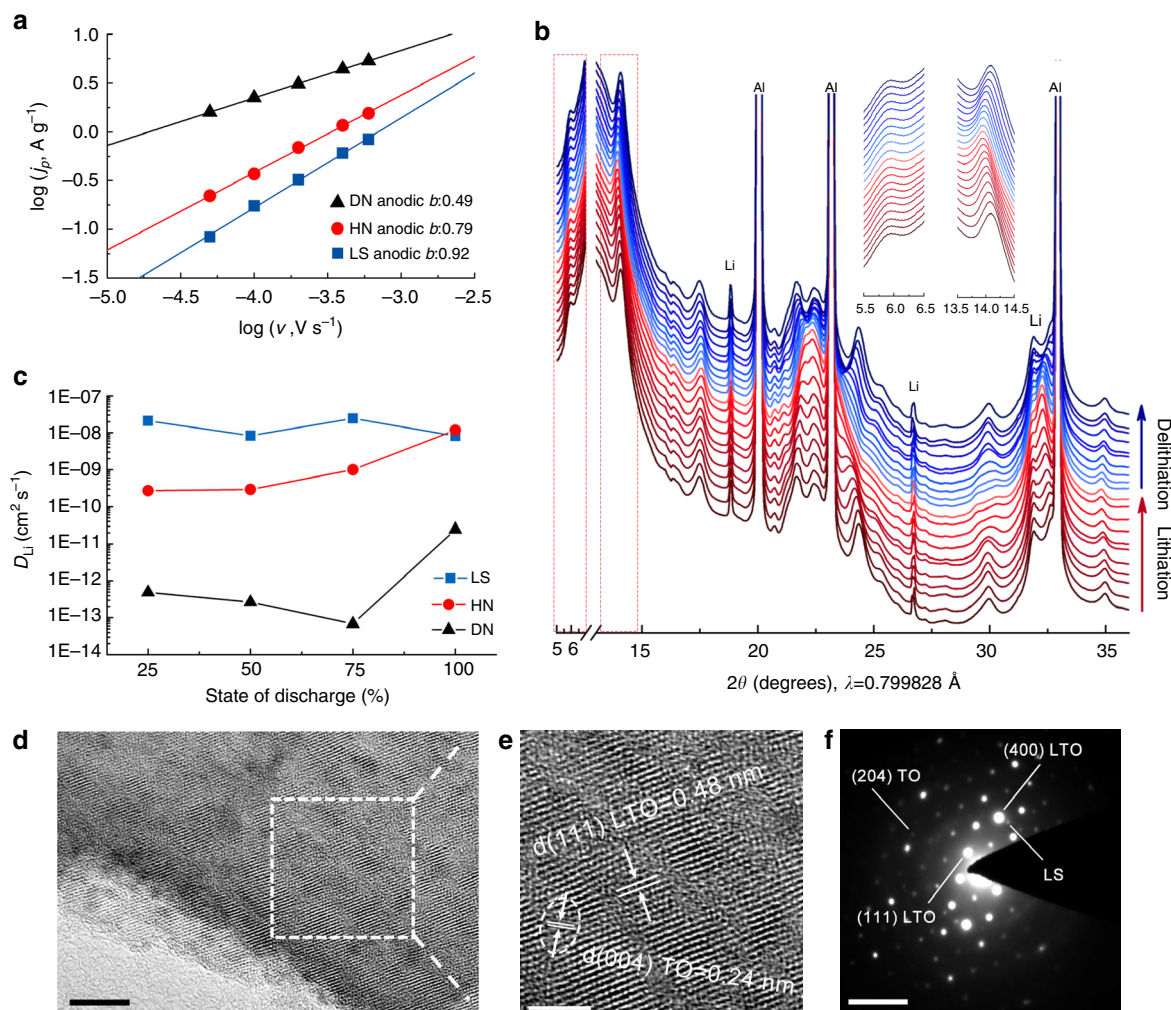
Fig. 4 Illustration for electrochemical performance enhancement mechanism of lithium titanate hydrates. **a**, b-values determination of anodic peaks with sweep rate from 0.05 mV s^{-1} to 0.6 mV s^{-1} for LS, HN and DN electrodes; **b** in situ synchrotron XRD results during the third cycle of LS electrode cycled at 100 mA g^{-1}, some main peaks of LS at 6° and 14° are highlighted in the insert; **c** Li-ion diffusion coefficient at various state of discharge; **d** HRTEM image of a HN nanosheet (scale bar, 10 nm) and **e** Magnified image of the selected region in **d** with a spacing of 0.48 nm of Li$_4$Ti$_5$O$_{12}$ and 0.24 nm of TiO$_2$ (scale bar, 5 nm); **f** SAED pattern of HN (scale bar, 5 1/nm)

the interfacial reactions between the electrodes and electrolyte, but with little influence on their performance[19]. The high rate capacity of DN at 4000 mA g^{-1}, in contrast, drops rapidly to < 20 mA h g^{-1} for the first 500 cycles, and failed completely after 1000 cycles. In terms of mass loading, rate and cyclability (see comparison with literatures in Supplementary Table 1), the HN and LS are two very promising materials (both hydrated) for fast-charging Li-ion batteries or even supercapacitors.

The charge storage mechanism was characterized by sweep voltammetry (Supplementary Fig. 18), assuming that the current obeys a power-law relationship with the sweep rate (Fig. 4a):[11, 12]

$$i = a v^b \qquad (1)$$

where a and b are adjustable parameters. For LS, b-value is 0.92, close to 1, indicating that the electrochemical kinetics is mainly generalized surface-controlled redox reaction. The b-value of DN, on the other hand, approaches a value of 0.5 (diffusion-controlled redox reaction). HN, as a combination of high-rate feature for faradic pseudocapacitance (LS) and high-capacity feature for diffusion-controlled process (Li$_4$Ti$_5$O$_{12}$ and TiO$_2$), presents an intermediate b-value of 0.79, and leads to the best capacity/cyclability combination (Supplementary Table 1).

The structural transformation of LS at different stages of extraction-insertion was examined via in situ synchrotron diffraction (Fig. 4b) at Argonne's Advanced Photon Source, demonstrating a solid-solution behavior[20] over a large concentration range. No two-phase transformation was detected, which involves changes of peak heights at distinct locations. The lattice constant (peak position) is seen to change linearly and reversibly with the state of charge. The change of interlayer spacing corresponding to ~6° is quite small, implying a fast transport kinetics of Li$^+$ through the layered structure. It is known that the solid solution behavior could emerge when increasing the (dis)charge rate or decreasing the particle size[20, 21]. Consequently, the fact that solid solution behavior appeared at relatively low current density (<0.5C) suggests that the electrode may possess good potential in achieving super high-rate capability[12, 22, 23]. The Li-ion diffusion coefficients (D_{Li}) of the three electrodes at different discharge depths are shown in Fig. 4c (see more details in Supplementary Table 4 and Supplementary Figs. 20, 22). The Li-ion diffusivity in LS (8.21×10^{-9}–2.46×10^{-8} cm^2 s^{-1}) is about 3–5 orders of magnitude higher than that in DN (6.81×10^{-14}–2.46×10^{-11} cm^2 s^{-1}). This tremendous difference is attributed to the nanostructure coarsening of DN and 2D layered structure of LS, which makes LS
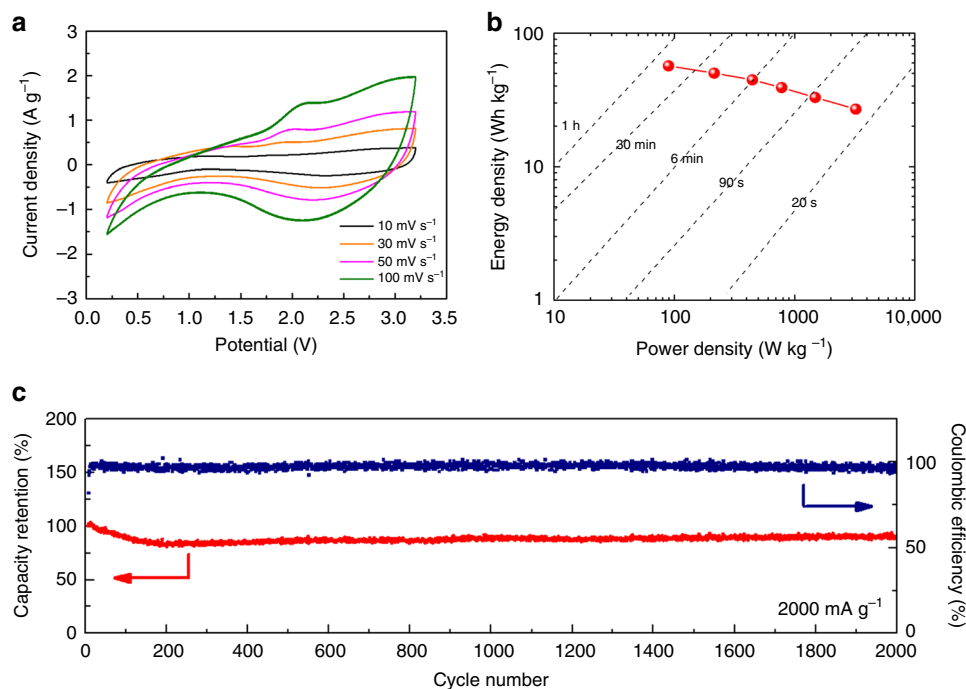
Fig. 5 Electrochemical performance of hybrid supercapacitor using an activated carbon (AC) and hydrated nanocomposite (HN) composite. **a**, CV curves in various scan rates from 10 to 100 mV s^{-1}; **b**, Ragone plots of power density vs. energy density, based on the total mass of active materials in both electrodes; **c**, Cycle stability and Coulombic efficiency at a current density of 2000 mA g^{-1}

a fast ion conductor. Just as shown in the animation and Fig. 4d, e, the HN was composed of uniformly dispersed $Li_4Ti_5O_{12}$ and TiO_2 crystallites about 2–5 nm on a LS nanosheet. Besides, the thickness of the HN nanosheets is only about 5 nm via atomic force microscope (AFM) analysis (Supplementary Fig. 23). Lattice fringes of anatase TiO_2 (004) plane and $Li_4Ti_5O_{12}$ (111) plane with a 40° angle are observed in Fig. 3d. Similarly, lattice fringes of anatase TiO_2 (004) plane and LS plane with a 28° angle (Supplementary Fig. 24) are also discovered. In selected-area electron diffraction pattern (SAED, Fig. 4f), the HN composite material was constituted by a set of sharp spots corresponding to (111), (311) and (400) planes of $Li_4Ti_5O_{12}$, some weak spots corresponding to (204) planes of anatase TiO_2 and unknown planes of LS, proving that it is a combination of LS and $Li_4Ti_5O_{12}$ monocrystals with minor amount of anatase TiO_2 monocrystals. As ion conductivity can be greatly enhanced by the space charge and percolation[24], hybrid nanostructured HN can exhibit outstanding Li-ion diffusion coefficients (2.72×10^{-10}–1.17×10^{-8} cm^2 s^{-1}).

HN composite (consisting of LS/LTO/TO mixture) during battery cycling was also examined using in situ synchrotron diffraction. In Supplementary Fig. 25, the diffraction peaks of the LS component show a continuous shift in small range during the lithiation/delithiation process, which demonstrates a solid-solution behavior. Interestingly, no obvious two-phase transitions were found in the in situ XRD pattern of the LTO and TO components either. It is well known that the redox mechanism of bulk LTO and TO involves two-phase transformations[17, 18, 25]. However, when the particle size decreases to several nanometers (<5 nm), many electrode materials with two-phase behavior will change to solid-solution behavior, showing a single solid-solution (such as regular solution model with nonzero enthalpy of mixing) phase field with large solubility range for Li[26, 27]. This would allow skipping the nucleation-and-growth kinetics of two-phase transformations, which involves an interfacial energy plus surface energy penalty

that could be too expensive and slow for small particles undergoing fast changes. Here, the capacitor-like behavior indeed demonstrates the nano-size effect of our HN nanocomposite material as well as the advantages of ODIN strategy, which leads to the best electrode with super high-rate capability.

ODIN is a simple approach to obtain sub-10 nm LTO/TO crystallites firmly anchored on LS. While nanocrystallites could more easily accommodate the structural changes during the ultrafast insertion and extraction process for the cycling stability improvement[28], a major problem is the aggregation of nanocrystallites during preparation and battery cycling[29]. The LS substrate plays a crucial role in structural anchoring to restrict the growth and prevent the aggregation of LTO and TO nanograins during RT battery cycling, thus making the ultrastable performance of HN possible. Lattice distortion and disorder in HN composite at the interfaces among LTO-TO-LS (Fig. 4e and Supplementary Fig. 26) and some disordered protons located in the interface layer (detected by ^{1}H solid state magic-angle spinning nuclear magnetic resonance (MAS-NMR), Supplementary Fig. 27) may provide more active sites for Li storage and more crystal defects for conductivity improvement[30–32]. In addition, when the size of a crystal decrease to several nanometers, not only is the diffusion distance of lithium ions shortened[33], the local material properties could even change as well[34, 35], which might greatly enhance the ionic and electrical conductivity of the crystal.

To demonstrate the practical utility of HN anode, we tested the electrochemical performance of hybrid supercapacitor using the commercial activated carbon (AC, YP-50F by Kuraray Chemical Co., LTD) and HN composite at an optimal mass ratio of $m_{positive}/m_{negative} = 3:1$, between 0.2 and 3.2 V. Different from the symmetric supercapacitor, the AC//HN hybrid supercapacitor exhibits a gradual deviation from the ideal rectangular shape with increasing scan rate (Fig. 5a), owing to the overlapping of two different energy-storage mechanisms. The Ragone plot (Fig. 5b), which exhibits the trade-off between energy and power densities

in the hybrid supercapacitor, was calculated from the cyclic voltammograms using the equations of Zhang et al[36] (the energy density and power density were based on the total mass of active materials in both electrodes). The hybrid supercapacitor not only could deliver up to 57 Wh kg^{-1} at relatively low-power density (90 W kg^{-1}), but also could maintain 27 Wh kg^{-1} with an extremely high-power density of about 3200 W kg^{-1} (fully charged within 30 s). It also exhibited an ultrastable cycling performance (2000 cycles with capacity fade of only 5×10^{-3} % per cycle) under a current density of 2000 mA g^{-1} (Fig. 5c), proving its ultrafast transport of both e$^-$ and Li$^+$ in aprotic electrolyte systems (Supplementary Movie 3). In addition, we have also assembled full batteries with LiFePO$_4$ cathode vs. HN anode (Supplementary Fig. 28), with tolerable gassing. The excellent cyclability of the full cell validates LTHs as promising electrode materials for the real-life fast-charging electronics and electric vehicles.

Discussion

In summary, we have discovered a series of novel lithium titanate hydrates in the Li$_2$O–TiO$_2$–H$_2$O ternary composition space. The LTHs exhibit outstanding high-rate performance, and even more intriguingly, extraordinary RT cycling stability. Once we realize that not all water is bad, and some water can actually do good, it might be possible to synthesize many more electrode materials with superior power density and ultralong cycle life in the Li$_2$O–TiO$_2$–H$_2$O composition space, that beat what are available on the Li$_2$O–TiO$_2$ binary axis (the "dry" side), by taking advantages of the structural diversity of hydrated crystals (2D layered), and dehydration induced phase transformation and nanostructure refinement.

The ODIN approach may be generalized to other hydrated compound composition spaces as well. The materials design philosophy we have established is the following: (i) water may not be bad actor for RT electrochemical cycling in aprotic electrolyte, if they are trapped in the lattice and not free (our empirical evidence is that the TG desorption temperature should be above 190 °C or so); (ii) as water promotes structural diversity in hydrothermal or sol-gel process, it could be used to tailor the initial structures such as 2D sheets or nanotubes, which greatly improves the ion diffusivity; (iii) the dehydration process thereafter should be carefully optimized: first, all the "free" water (adsorbed, crystallographic) should be driven out; but as it is not integral part of the lattice, this usually does not cause drastic phase change. Then as temperature is further raised, some pseudohydrates embedded in the lattice are also partially driven out; as they were strongly embedded in the lattice, their partial removal can cause drastic phase transformation. This is actually a golden opportunity to refine the nanostructures, as the old structure is being dismantled and turned into a defected form, and new phases are nucleated as nanocrystals, which must start out very small by definition. These sub-10 nm new phases are well-anchored on the 2D substrate, providing structural stability during high-rate RT cycling, as well as a hybrid supercapacitor-battery kinetics and the best capacity/rate/cyclability combination. Because of this, we believe in many occasions after hydrothermal or sol-gel processing, there could exist an optimal dehydration temperature $T_{optimal}$ for achieving the best RT electrochemical performance. Further drying the system above $T_{optimal}$ will be counter-productive, since the nanostructures could (i) aggregate and coarsen, (ii) or change from 2D to 3D forms, as we showed for the case of DN, where not only the rate capability degrades, but also the cyclability. As ubiquitous water is in nature and in chemical synthesis, we believe the ODIN synthetic approach could provide a window

of opportunity for finding new high-performance electrode materials in aprotic electrolyte systems.

Methods

Materials synthesis. A typical preparation procedure of lithium titanate hydrates consists of three steps. First, layered hydrogen trititanate was prepared via hydrothermal reaction between anatase TiO$_2$ powders and concentrated NaOH solution at 150 °C for several hours, followed by ion substitution of Na$^+$ with H$^+$ in 0.5 M HNO$_3$ solution for 3 h. Second, layered LTHs-precursor was obtained by chemical lithiation of hydrogen trititanate in a 0.8 M LiOH solution heated at 150 °C for 12 h in a Teflon-lined stainless steel autoclave. Thirdly, a series of lithium titanate hydrates were synthesized by drying the LTHs-precursor at various temperatures ranging from 80 to 400 °C for 3 h in a vacuum. In this article, LS and HN were obtained at 190 and 260 °C, respectively. For comparison, we chose 800 °C as the synthesis temperature for DN, and kept the other heating experimental variables fixed.

Materials characterization. Ex situ powder X-ray diffraction (XRD) was recorded on a Bruker D8 Advance with Cu Kα radiation (λ = 1.5418 Å). In situ XRD measurements were carried out at 11-ID-C beamline (for the dehydration process of LTHs-precursor and the charge and discharge process of HN) and 11-ID-D beamline (for the charge and discharge process of LS) at Advanced Photon Source, Argonne National Laboratory. Scans were collected in transmission mode using fixed wavelengths of 0.10798/0.117418 and 0.799828 Å for 11-ID-C beamline and 11-ID-D beamline, respectively. The 2D patterns were calibrated and converted to the conventional 1D format (intensity vs. 2 theta) by using the GSAS-II program. The data are plotted and analyzed by using Bachir Aoun's Ranked Data Analysis program[37]. For the dehydration, the LTHs-precursor was heated up to 400 °C with a heating rate of 2 °C min^{-1} and a spectrum data collection of one pattern every 60 s. For the charge and discharge process, a coin-cell with a hole for beam path was assembled using the same electrode and electrolyte mentioned below. Thermogravimetric-differential scanning calorimetry (TG-DSC) analysis was carried out using NETZSCH-STA 449 F3 with a heating rate of 2 °C min^{-1} under a continuous flow of Ar (100 ml min^{-1}). Inductively coupled plasma mass spectroscopy (ICP-MS) analysis was carried out using iCP QC (Thermo Fisher Scientific, USA) for lithium and titanium content, and elemental analyzer (EuroEA3000) was used for hydrogen and oxygen content. For Ti analysis, as it is difficult to dissolve in HNO$_3$, HF was used as the solvent, and the test was repeated three times. X-ray photoelectron spectroscopy (XPS) spectra were obtained using Escalab 250XI system (Thermo Fisher Scientific, US). Nitrogen adsorption–desorption isotherms were obtained using an Automated vapor sorption analyzer (Autosorb-iQ2-MP (Quanta Chrome)) at 77.4 K under vacuum. The specific surface area was calculated by the Brunauer-Emmett-Teller (BET) method. The morphology, size and crystal structure of the as-prepared samples were characterized by MERLIN VP Compact for scanning electron microscope (SEM), Hitachi-HT7700 for transmission emission microscopy (TEM), JEM-2100F for high-resolution transmission electron microscopy (HRTEM) and selected-area electron diffraction (SAED). Tapping mode atomic force microscopy (AFM) images were collected on a multimode atomic force microscope from Veeco Instruments, employing Olympus microcantilevers (resonance frequency, 300 kHz; force constant, 42 N m^{-1}). ^{1}H solid state magic-angle spinning nuclear magnetic resonance (MAS-NMR) spectra was performed on a Bruker Avance III (400 MHz) spectrometer equipped with a triple channel 2.5 mm probe and adamantine was used as reference. The data were recorded using a pulse sequence with the spinning speed of 10K. The samples were prepared and measured after drying over night at 70 °C in a vacuum. Infrared spectra of the powder samples were measured in diffuse reflectance using a Bruker TENSOR II spectrometer. The samples were measured against a KBr background after purging in inert gas to remove gas-phase water. The depth profiling of LTHs was also analyzed by time-of-flight secondary ion mass spectrometry (TOF-SIMS) using dual ion beams TOF-SIMS (TOF.SIMS 5), in which the Cs$^+$ ions are for sputtering and the Bi$_1^+$ ions are for analysis.

Electrochemical measurements. For the electrochemical measurements, the working electrode was prepared by mixing 80 wt% active material, 10 wt% Super P, and 10 wt% poly(vinylidene fluoride) binder in N-methyl-2-pyrrolidinone solvent. The obtained slurry was cast on 16 µm thickness Al foil or 15 µm thickness Cu foil (when HN was prepared as anode in hybrid supercapacitor and full batteries) via scraper machine and dried at 110 °C in a vacuum oven for 12 h. Then roll squeezer was used to enhance the contact between material and foil, together with increasing the compaction density. The 2032-coin-type cells were assembled in an argon-filled glove-box using pure lithium foil (for half cells) or commercial activated carbon (YP-50F by Kuraray Chemical Co., LTD for hybrid supercapacitors) or commercial LiFePO$_4$ (for full cells) as counter electrodes, and a microporous membrane (Celgard 2400, USA) as a separator. 80 µL of 1.0 M LiPF$_6$ in a mixture (1:1 volume ratio) of ethylene carbonate (EC) and dimethylcarbonate (DMC) was added as the electrolyte. The mass loading of LTHs anode in this work is ~1.0 mg cm^{-2}. In hybrid supercapacitor device, the AC cathode is about triple the mass of anode; and in the full batteries, the LiFePO$_4$ cathode is about twice the mass of anode. IM6 (Bas-Zahner, Germany) electrochemical workstation was used for

cyclic voltammetry (CV) and also for electrochemical impedance spectroscopy (EIS) from 10 mHz to 100 kHz, with a perturbation of 5 mV applied. For in situ XRD measurements, the home-made coin cell (LS on Al foil) was discharged/charged with a constant current at 100 mA g^{-1}. All the cells were tested on a LAND 2001A Cell test system and cycled between 1.0–2.5 V (for half cells), 0.2–3.2 V (for hybrid supercapacitors) and 1.2–2.4 V (for full cells) at room temperature.

References

1. Dunn, B., Kamath, H. & Tarascon, J. Electrical energy storage for the grid: a battery of choices. *Science* **334**, 928–935 (2011).
2. Sun, Y. et al. Nanostructured high-energy cathode materials for advanced lithium batteries. *Nat. Mater.* **11**, 942–947 (2012).
3. Chen, Z., Belharouak, I., Sun, Y. K. & Amine, K. Titanium-based anode materials for safe lithium-ion batteries. *Adv. Funct. Mater.* **23**, 959–969 (2013).
4. Zhu, G. N., Wang, Y. G. & Xia, Y. Y. Ti-based compounds as anode materials for li-ion batteries. *Energy Environ. Sci.* **5**, 6652–6667 (2012).
5. Wang, L. & Sasaki, T. Titanium oxide nanosheets: graphene analogues with versatile functionalities. *Chem. Rev.* **114**, 9455–9486 (2014).
6. Zhao, B., Ran, R., Liu, M. & Shao, Z. A comprehensive review of Li$_4$Ti$_5$O$_{12}$-based electrodes for lithium-ion batteries: the latest advancements and future perspectives. *Mat. Sci. Eng. R.* **98**, 1–71 (2015).
7. Kawamura, T., Okada, S. & Yamaki, J. Decomposition reaction of LiPF$_6$-based electrolytes for lithium ion cells. *J. Power Sources* **156**, 547–554 (2006).
8. Hong, Z. S. & Wei, M. D. Layered titanate nanostructures and their derivatives as negative electrode materials for lithium-ion batteries. *J. Mater. Chem. A* **1**, 4403–4414 (2013).
9. Cho, G. Y., Wu, Y. T. & Ackerman, J. L. Detection of hydroxyl ions in bone mineral by solid-state nmr spectroscopy. *Science* **300**, 1123–1127 (2003).
10. Franks, F., Falk, M. & Knop, O. *Water in Stoichiometric Hydrates*. (ed. Franks, F.) 55–113 (Springer US, 1973).
11. Simon, P., Gogotsi, Y. & Dunn, B. Where do batteries end and supercapacitors begin? *Science* **343**, 1210–1211 (2014).
12. Augustyn, V. et al. High-rate electrochemical energy storage through Li$^+$ intercalation pseudocapacitance. *Nat. Mater.* **12**, 518–522 (2013).
13. Li, J. R., Tang, Z. L. & Zhang, Z. T. H-titanate nanotube: a novel lithium intercalation host with large capacity and high rate capability. *Electrochem. Commun.* **7**, 62–67 (2005).
14. Wen, P., Ishikawa, Y., Itoh, H. & Feng, Q. Topotactic transformation reaction from layered titanate nanosheets into anatase nanocrystals. *J. Phys. Chem. C* **113**, 20275–20280 (2009).
15. Chiu, H. et al. Annealing-regulated elimination of residual strain-induced structural relaxation for stable high-power Li$_4$Ti$_5$O$_{12}$ nanosheet anodes. *Nano Energy* **32**, 533–541 (2017).
16. Chen, X. B., Liu, L., Yu, P. Y. & Mao, S. S. Increasing solar absorption for photocatalysis with black hydrogenated titanium dioxide nanocrystals. *Science* **331**, 746–750 (2011).
17. Wagemaker, M., Borghols, W. J. H. & Mulder, F. M. Large impact of particle size on insertion reactions. a case for anatase Li$_x$TiO$_2$. *J. Am. Chem. Soc.* **129**, 4323–4327 (2007).
18. Borghols, W. J. H. et al. Size effects in the Li$_{4+x}$Ti$_5$O$_{12}$ spinel. *J. Am. Chem. Soc.* **131**, 17786–17792 (2009).
19. Chiu, H. et al. Capacity fade mechanism of Li$_4$Ti$_5$O$_{12}$ nanosheet anode. *Adv. Energy Mater* **7**, 1601825 (2016).
20. Liu, H. et al. Capturing metastable structures during high-rate cycling of LiFePO$_4$ nanoparticle electrodes. *Science* **344**, 1252817 (2014).
21. Zhang, X. et al. Rate-induced solubility and suppression of the first-order phase transition in olivine LiFePO$_4$. *Nano Lett.* **14**, 2279–2285 (2014).
22. Malik, R., Zhou, F. & Ceder, G. Kinetics of non-equilibrium lithium incorporation in LiFePO$_4$. *Nat. Mater.* **10**, 587–590 (2011).
23. Shirpour, M., Cabana, J. & Doeff, M. Lepidocrocite-type layered titanate structures: new lithium and sodium ion intercalation anode materials. *Chem. Mater.* **26**, 2502–2512 (2014).
24. Maier, J. Nanoionics: ion transport and electrochemical storage in confined systems. *Nat. Mater.* **4**, 805–815 (2005).
25. Ganapathy, S. & Wagemaker, M. Nanosize storage properties in spinel Li$_4$Ti$_5$O$_{12}$ explained by anisotropic surface lithium insertion. *ACS Nano* **6**, 8702–8712 (2012).
26. Niu, J. et al. In situ observation of random solid solution zone in LiFePO$_4$ electrode. *Nano Lett.* **14**, 4005–4010 (2014).
27. Wagemaker, M. et al. A kinetic two-phase and equilibrium solid solution in spinel Li$_{4+x}$Ti$_5$O$_{12}$. *Adv. Mater.* **18**, 3169 (2006).
28. Guo, Y., Hu, J. & Wan, L. Nanostructured materials for electrochemical energy conversion and storage devices. *Adv. Mater.* **20**, 2878–2887 (2008).
29. Wang, K., Li, X. & Chen, J. Surface and interface engineering of electrode materials for lithium-ion batteries. *Adv. Mater.* **27**, 527–545 (2015).
30. Wu, Q. et al. Ultrathin anatase TiO$_2$ nanosheets embedded with TiO$_2$-B nanodomains for lithium-ion storage: capacity enhancement by phase boundaries. *Adv. Energy Mater* **5**, 1401756 (2014).
31. Magasinski, A. et al. High-performance lithium-ion anodes using a hierarchical bottom-up approach. *Nat. Mater.* **9**, 353–358 (2010).
32. Xia, T. et al. Hydrogenated surface disorder enhances lithium ion battery performance. *Nano Energy* **2**, 826–835 (2013).
33. Kang, B. & Ceder, G. Battery materials for ultrafast charging and discharging. *Nature* **458**, 190–193 (2009).
34. Fernández-García, M., Martínez-Arias, A., Hanson, J. C. & Rodriguez, J. A. Nanostructured oxides in chemistry: characterization and properties. *Chem. Rev.* **104**, 4063–4104 (2004).
35. Chen, X. & Mao, S. S. Titanium dioxide nanomaterials: synthesis, properties, modifications, and applications. *Chem. Rev.* **107**, 2891–2959 (2007).
36. Zhang, F. et al. A high-performance supercapacitor-battery hybrid energy storage device based on graphene-enhanced electrode materials with ultrahigh energy density. *Energy Environ. Sci.* **6**, 1623–1632 (2013).
37. Aoun, B. et al. A generalized method for high throughput in-situ experiment data analysis: an example of battery materials exploration. *J. Power Sources* **279**, 246–251 (2015).

Author contributions

Z.T. and Ju.L.: Conceived the project. S.W. and W.Q.: Synthesized samples and performed electrochemical tests. S.W., Z.Z., Y.Y., Q.L. Y.R., X.Z., R.X. and Jun.L.: Performed the characterization. All authors analyzed the data and contributed to the discussion. S.W., Z.T. and Ju.L.: Wrote the manuscript.

Description of Supplementary Files

File name: Supplementary Information

Description: Supplementary figures, supplementary tables, supplementary notes and supplementary references.
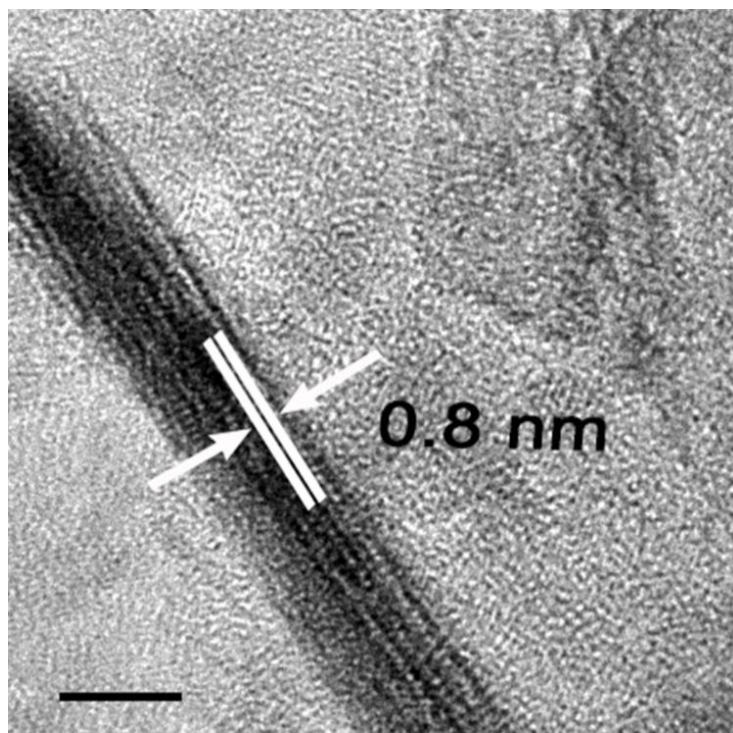
File name: Supplementary Movie 1

Description: Animation of ODIN approach in $Li_2O-TiO_2-H_2O$ ternary composition space
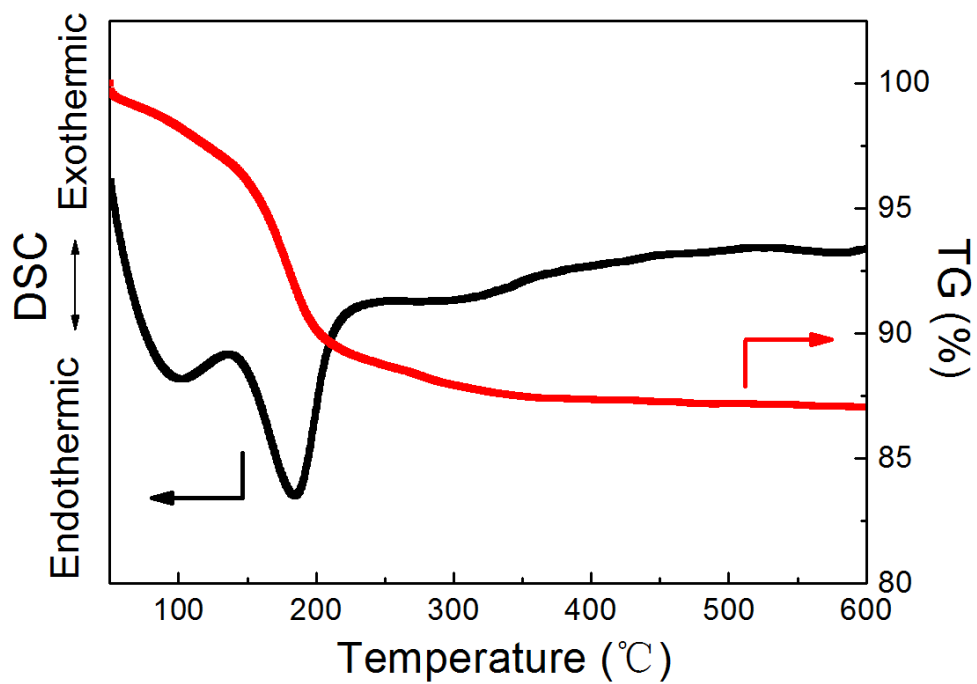
File name: Supplementary Movie 2

Description: Animation of ODIN approach on a nanoscale
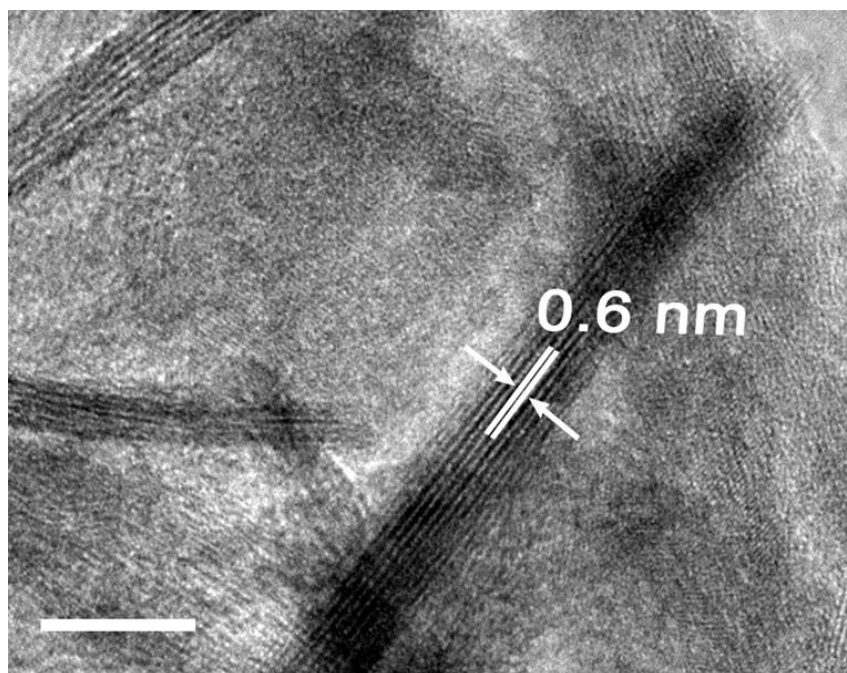
File name: Supplementary Movie 3

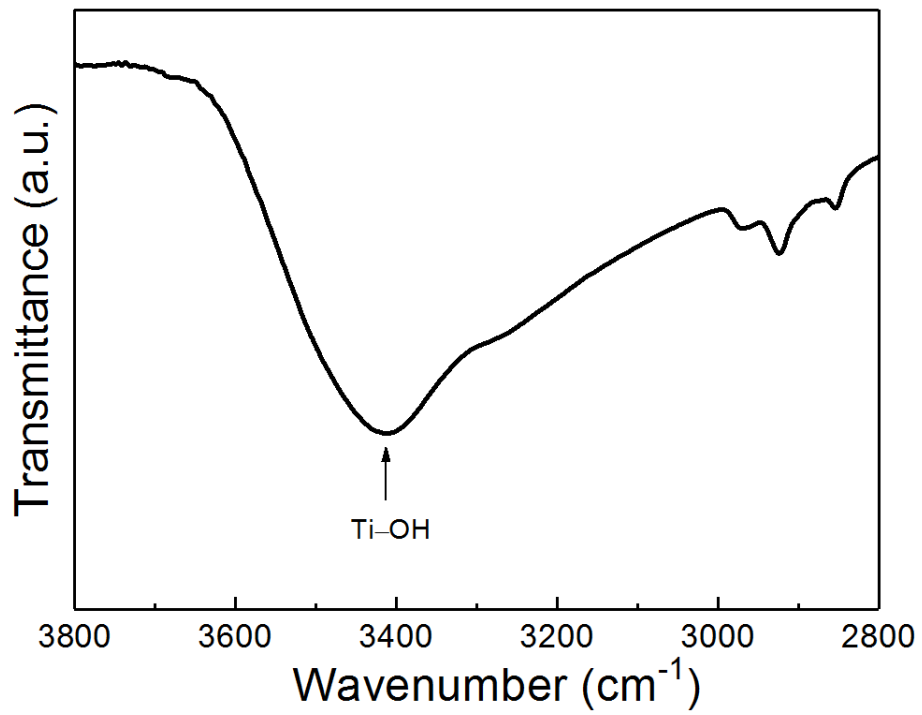Description: Animation of lithium titanate hydrates in battery

Supplementary Figure 1 | HRTEM image of lithium titanate hydrates precursor (*LTHs-precursor*). *Scale bar*, 5 nm.
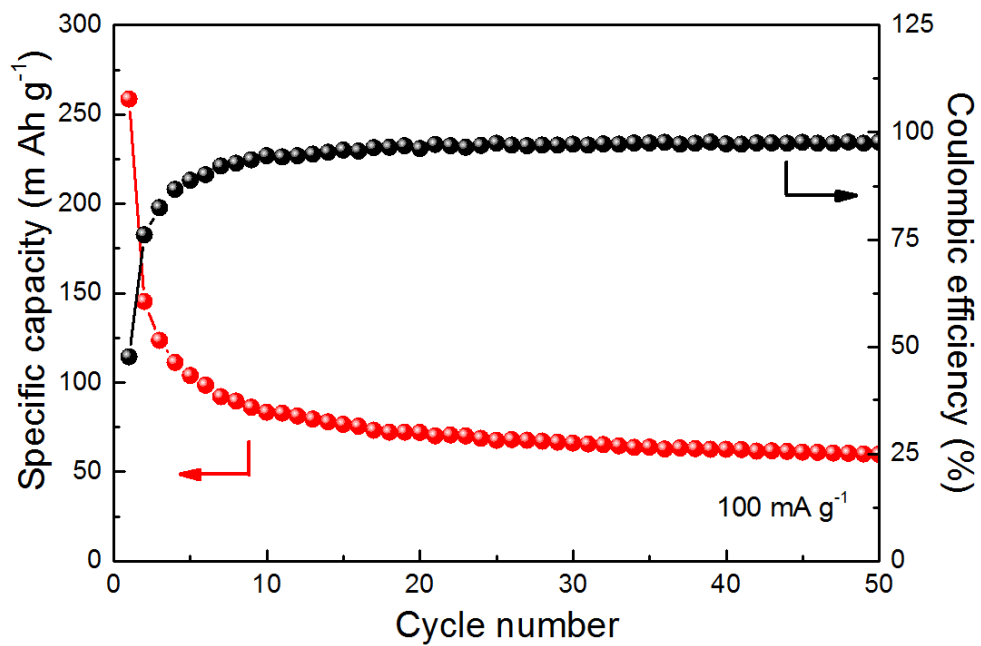
Supplementary Figure 2 | TG-DSC curves of lithium titanate hydrates precursor (*LTHs-precursor*).
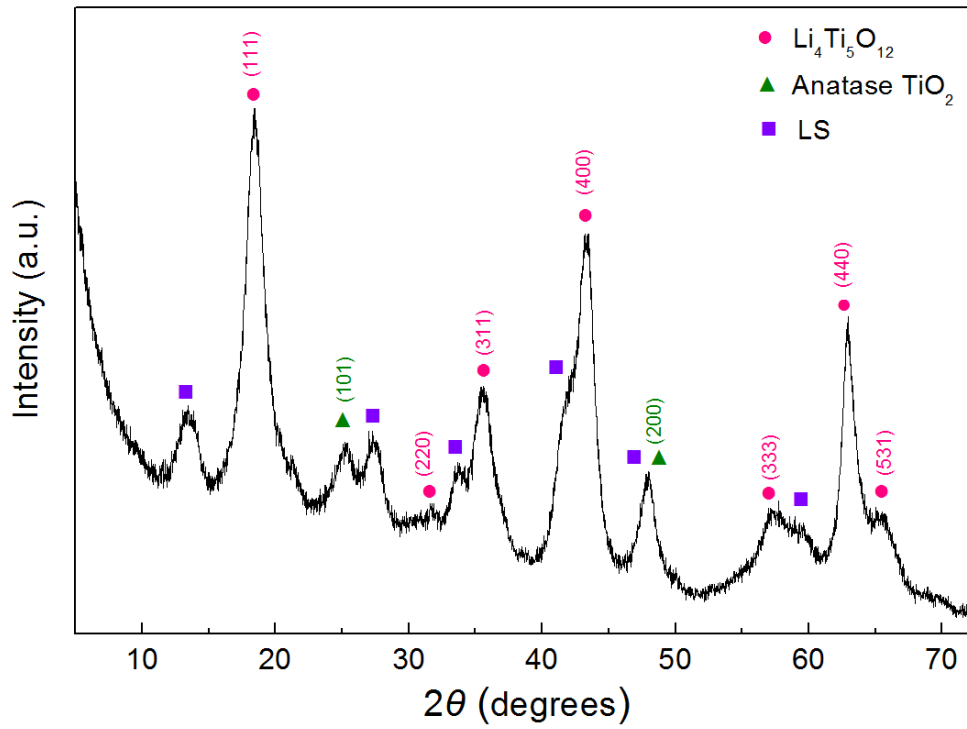
Supplementary Figure 3 | HRTEM image of layered structure (*LS*). *Scale bar*, 10 nm.
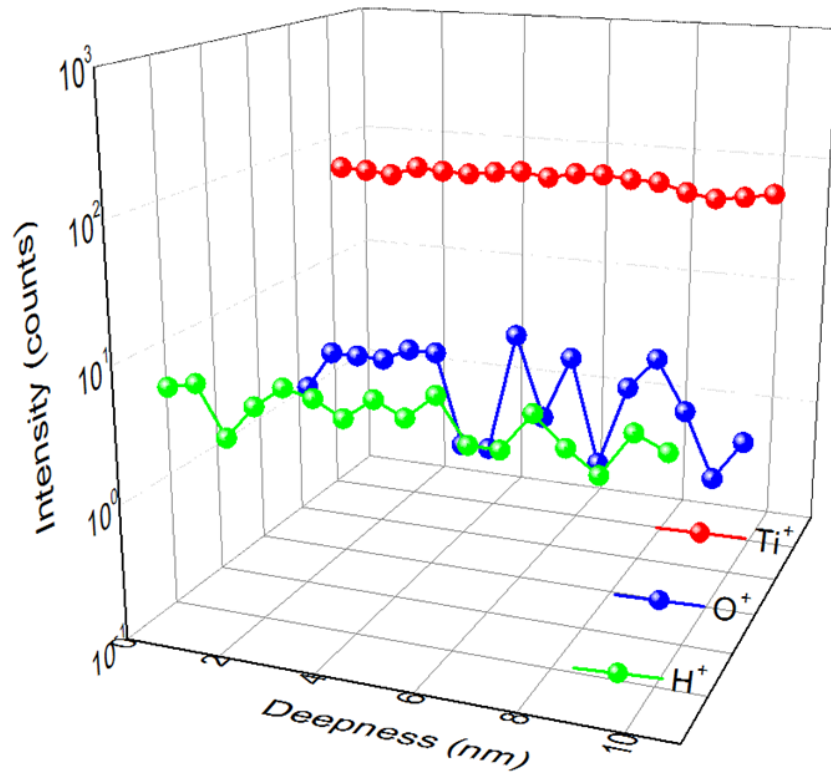
Supplementary Figure 4 | FTIR spectra of layered structure (*LS*).
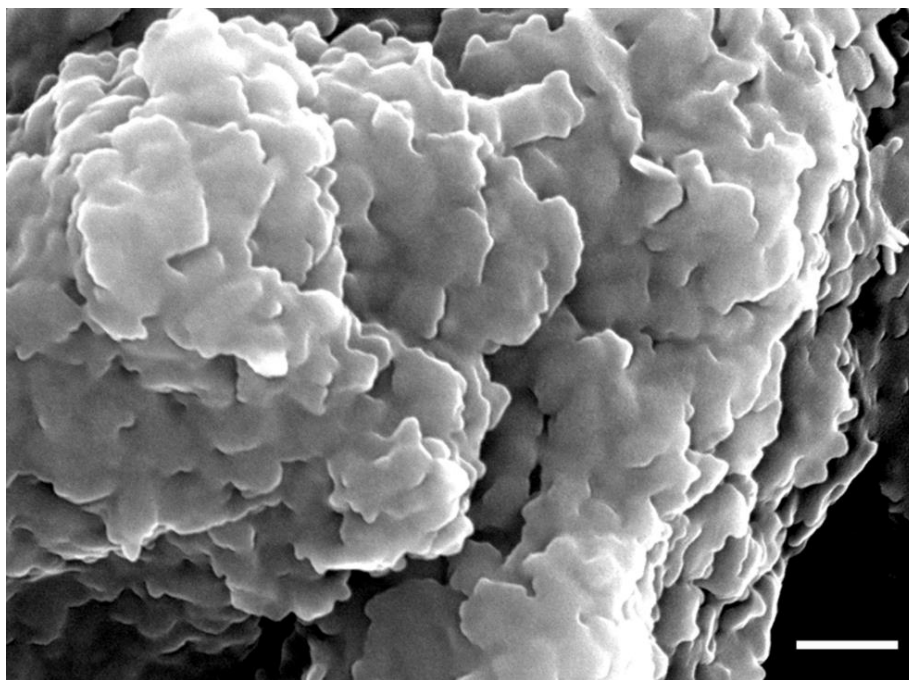
Supplementary Figure 5 | Cycling stability and Coulombic efficiency of lithium titanate hydrates precursor (*LTHs-precursor*) at 100 mA g⁻¹.

Supplementary Figure 6 | XRD patterns of hydrated nanocomposite (*HN*) with the individual sets of planes indexed.

Supplementary Figure 7 | TOF-SIMS profile of a 10 nm thick hydrated nanocomposite (*HN*) nanosheet.

Supplementary Figure 8 | SEM image of layered structure (*LS*). *Scale bar*, 200 nm.
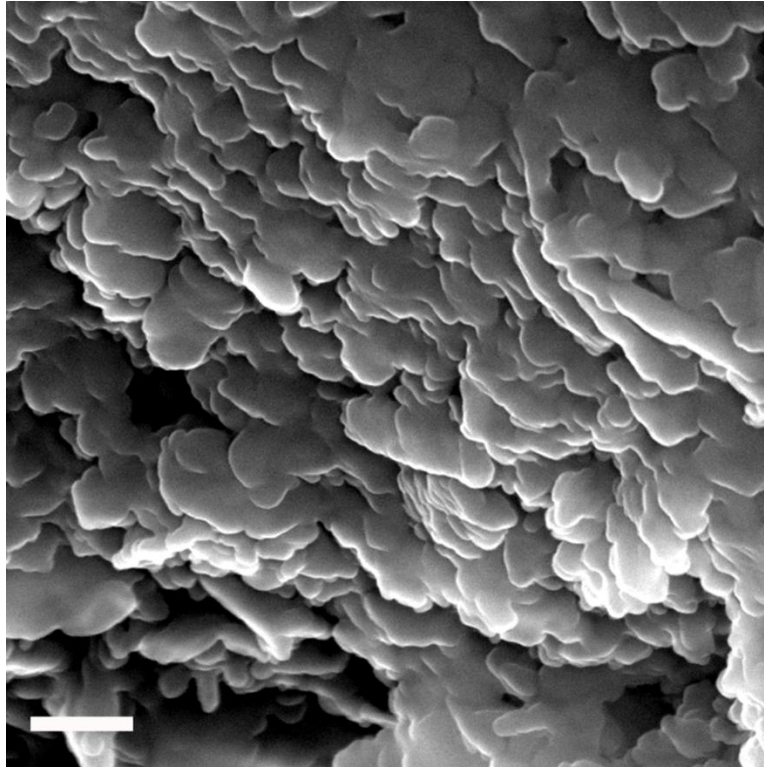
Supplementary Figure 9 | SEM image of hydrated nanocomposite (*HN*). *Scale bar*, 200 nm.
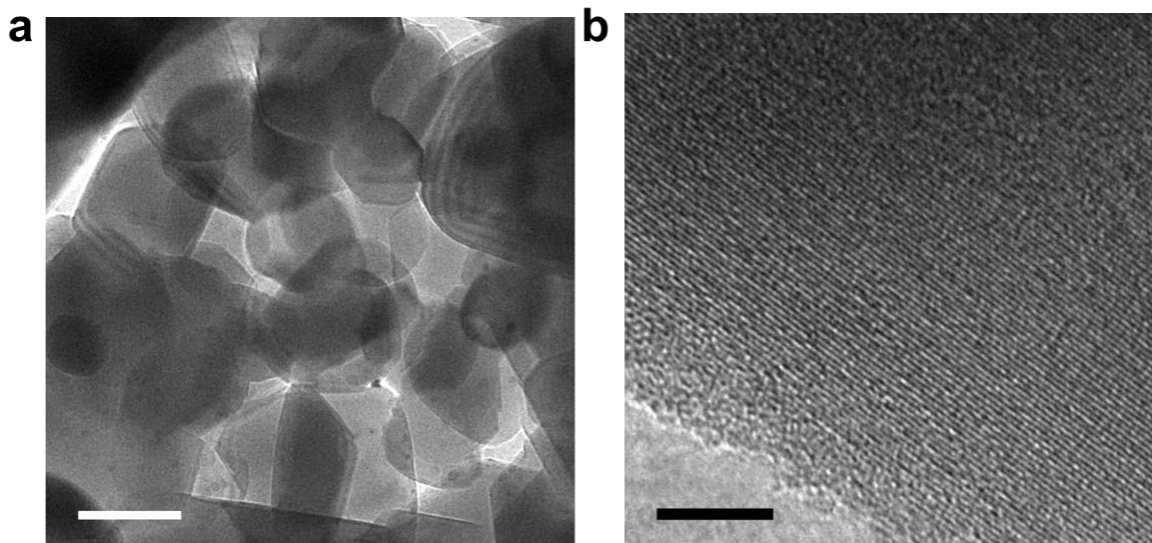
Supplementary Figure 10 | HRTEM images of dry nanocomposite (*DN*). *Scale bar*, 100 nm (a), 5 nm (b).
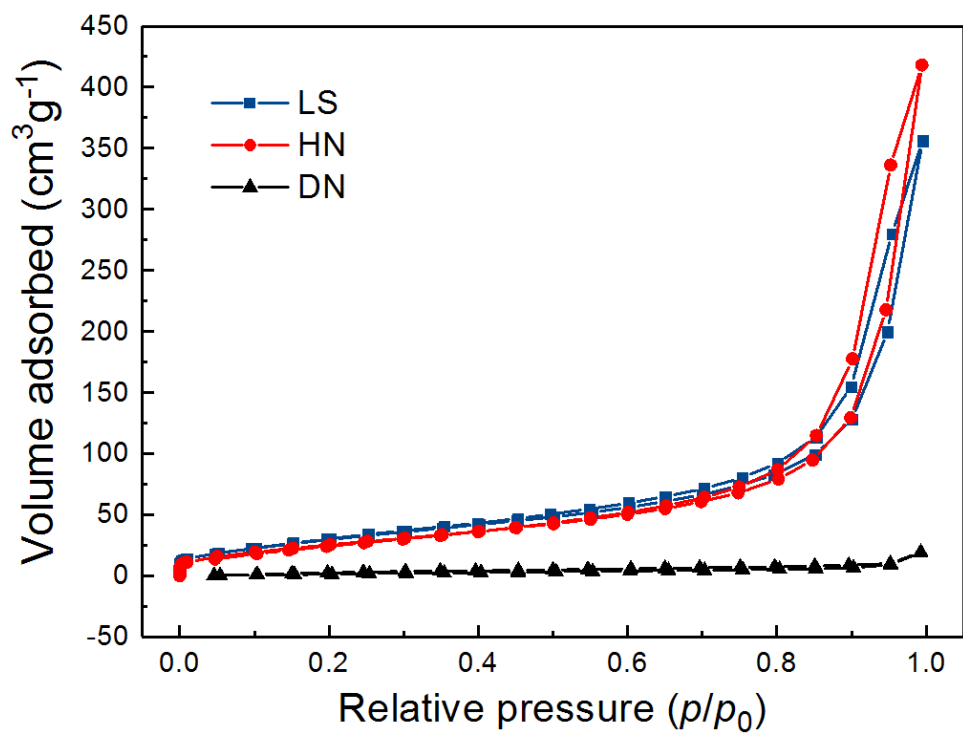
Supplementary Figure 11 | N₂ adsorption/desorption isotherms of layered structure (*LS*), hydrated nanocomposite (*HN*) and dry nanocomposite (*DN*).
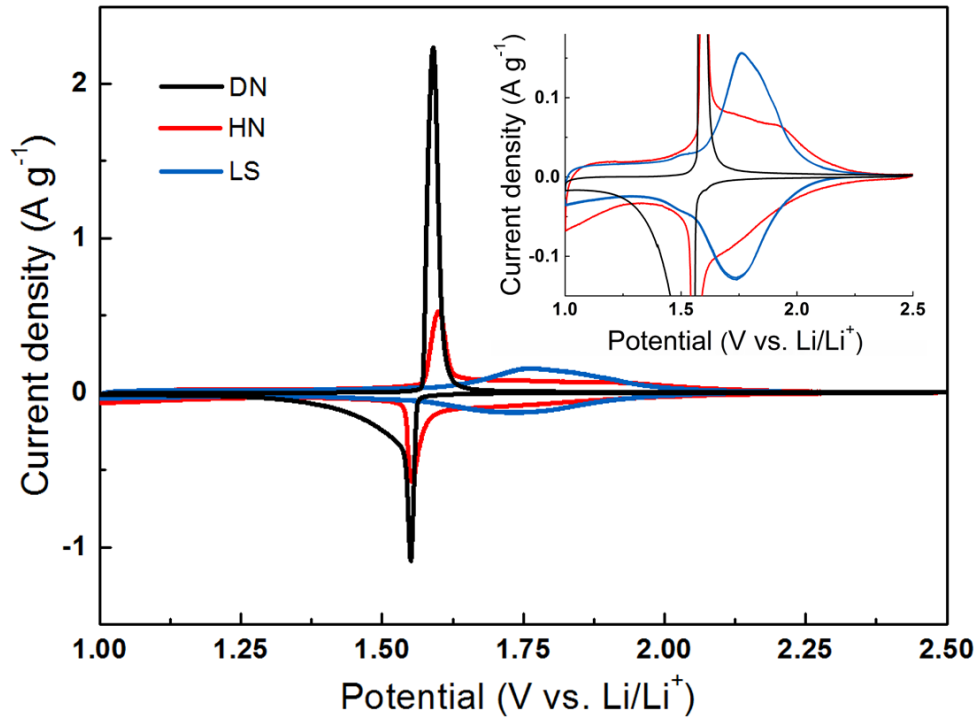
Supplementary Figure 12 | Cyclic voltammetry curves at 0.1 mV s⁻¹ for comparison among layered structure (*LS*), hydrated nanocomposite (*HN*) and dry nanocomposite (*DN*) electrode materials.
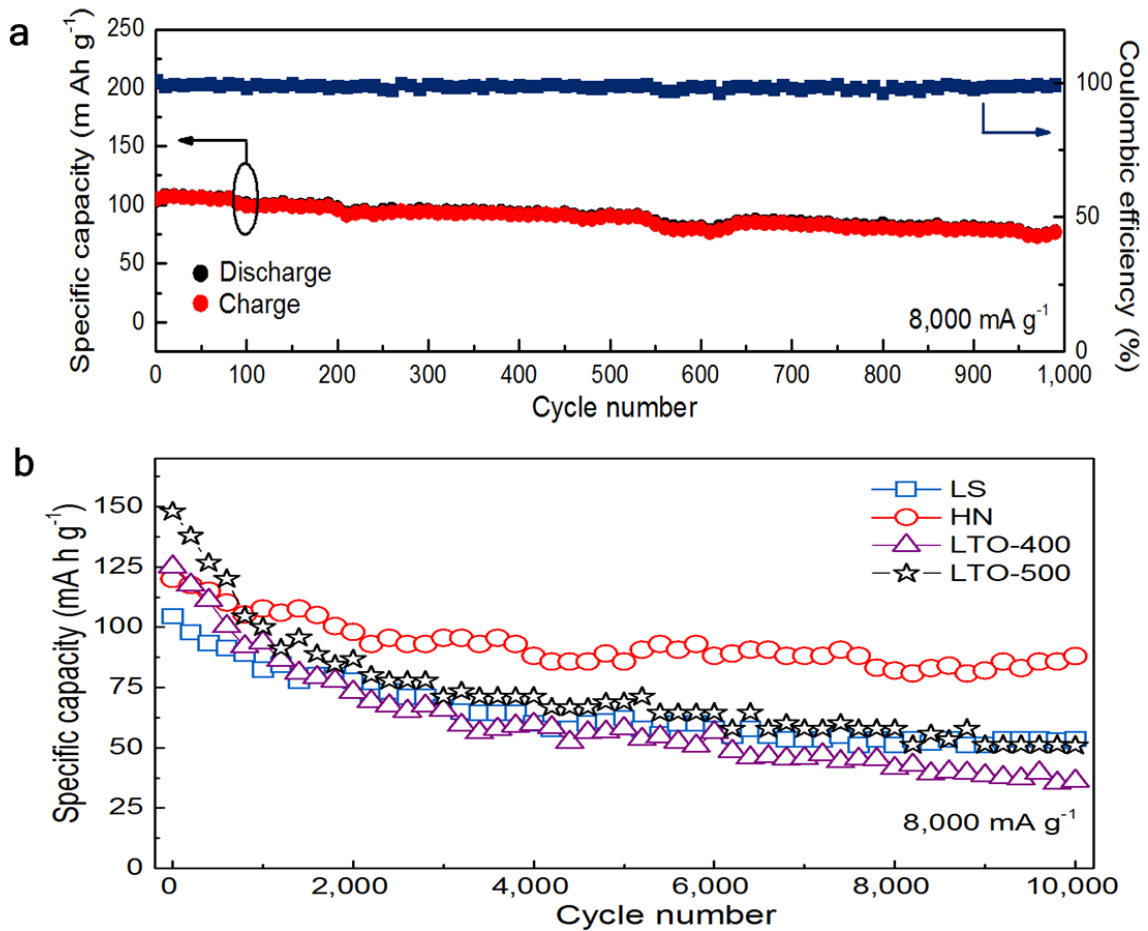
Supplementary Figure 13 | Electrochemical performances of as-synthesized electrode materials. (a) Cycling stability and Coulombic efficiency of layered structure (*LS*) electrodes and (b) the comparison of cycling performances at current density of 8,000 mA g^{-1}.
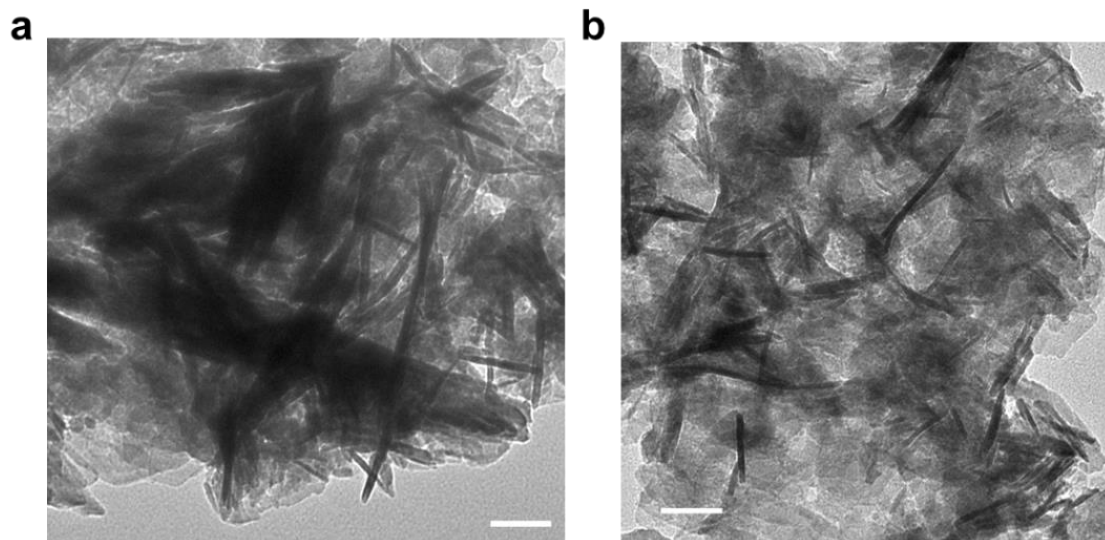
Supplementary Figure 14 | TEM images of hydrated nanocomposite (*HN*) after 10,000 cycles.
Scale bar, 50 nm (a, b).
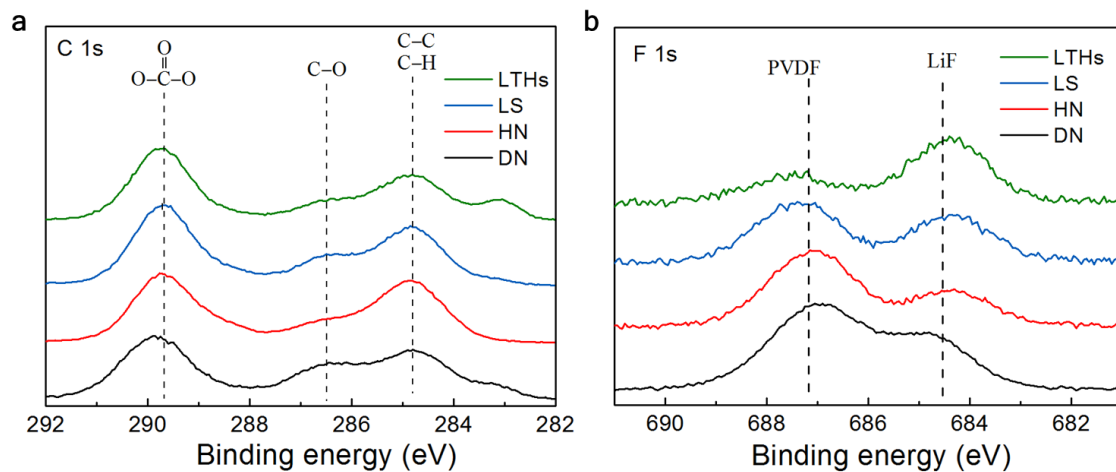
Supplementary Figure 15 | XPS spectra analysis of as-synthesized electrodes. C 1s (a) and F 1s (b) XPS spectra of lithium titanate hydrates (*LTHs*), layered structure (*LS*), hydrated nanocomposite (*HN*) and dry nanocomposite (*DN*) electrodes after 10,000 cycles at 4,000 mA g^{-1}.
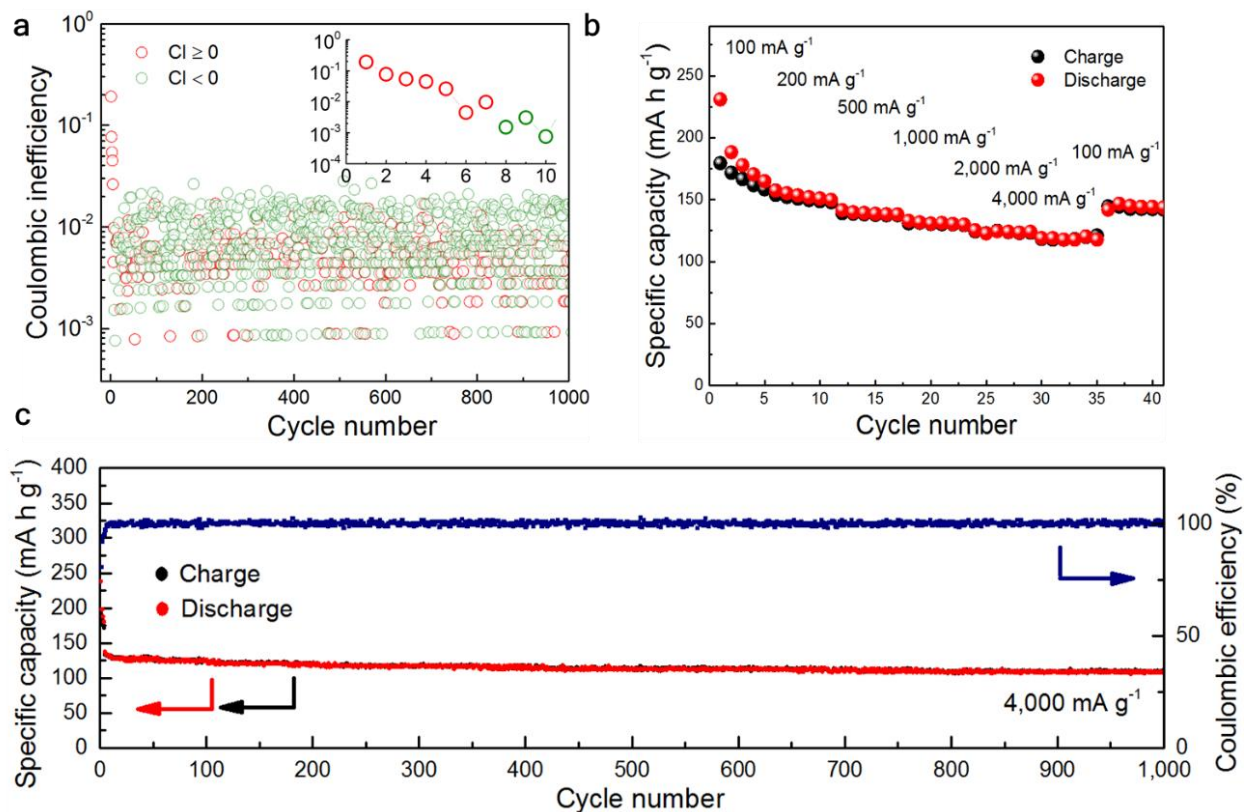
Supplementary Figure 16 | Electrochemical performances of hydrated nanocomposite (*HN*) when 1M LiTFSI in EC and DMC (1:1 by volume) was chosen as the electrolyte. (a) Coulombic inefficiency at 4,000 mA g⁻¹, the insert magnifies Coulombic inefficiency for the first 10 cycles; (b) The rate performances and (c) Cycle stability and Coulombic efficiency at 4,000 mA g⁻¹.
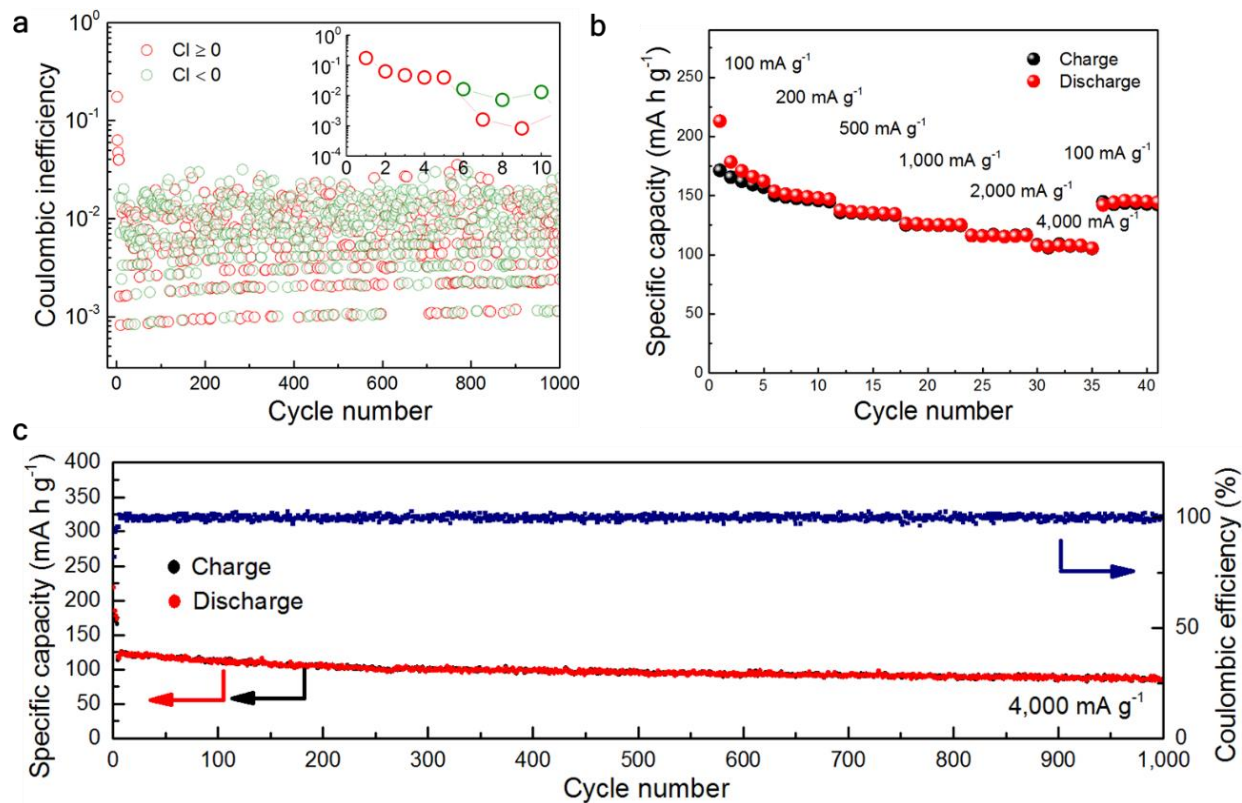
Supplementary Figure 17 | Electrochemical performances of layered structure (*LS*) when 1M LiTFSI in EC and DMC (1:1 by volume) was chosen as the electrolyte. (a) Coulombic inefficiency at 4,000 mA g^{-1}, the insert magnifies Coulombic inefficiency for the first 10 cycles; (b) The rate performances and (c) Cycle stability and Coulombic efficiency at 4,000 mA g^{-1}.
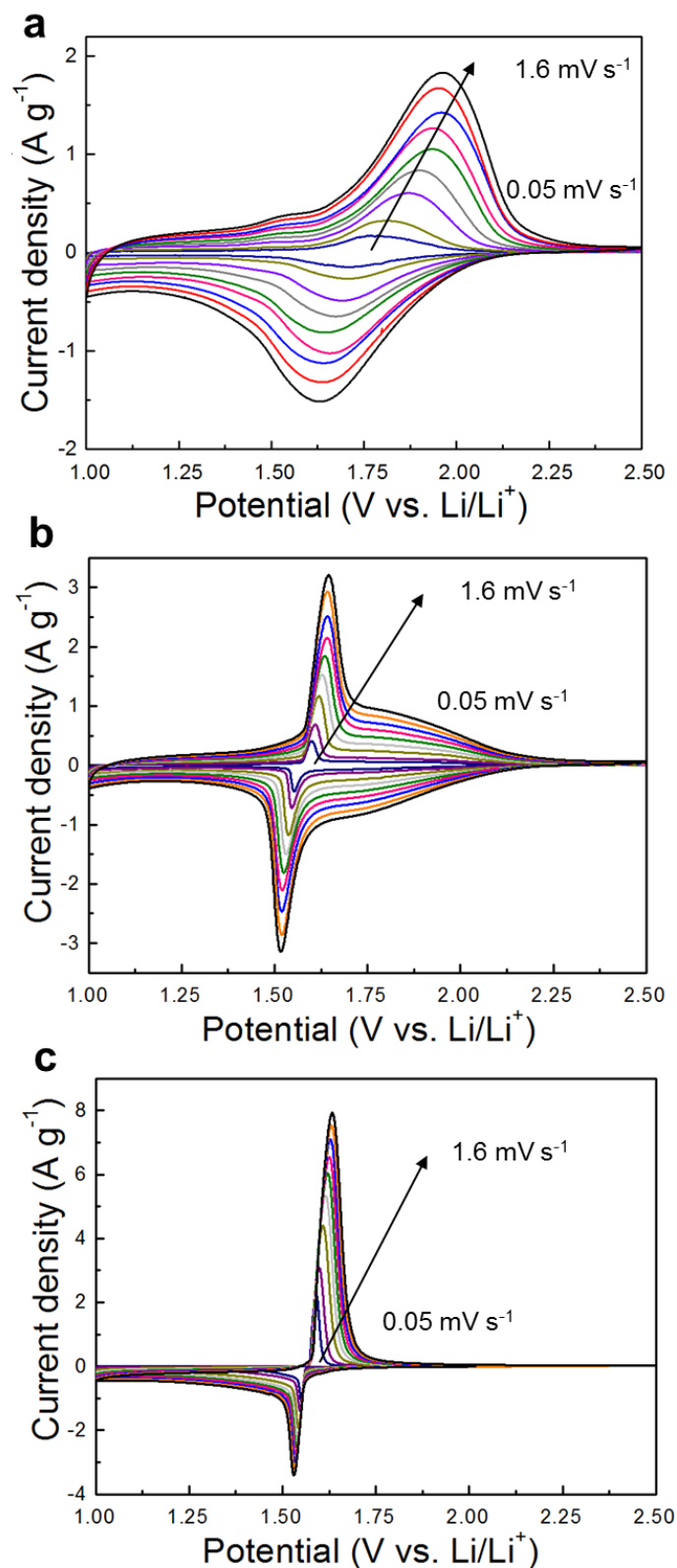
Supplementary Figure 18 | Cyclic voltammetry curves of as-synthesized electrodes from 0.05 to 1.6 mV s⁻¹. (a) Layered structure (*LS*), (b) hydrated nanocomposite (*HN*) and (c) dry nanocomposite (*DN*) electrodes.
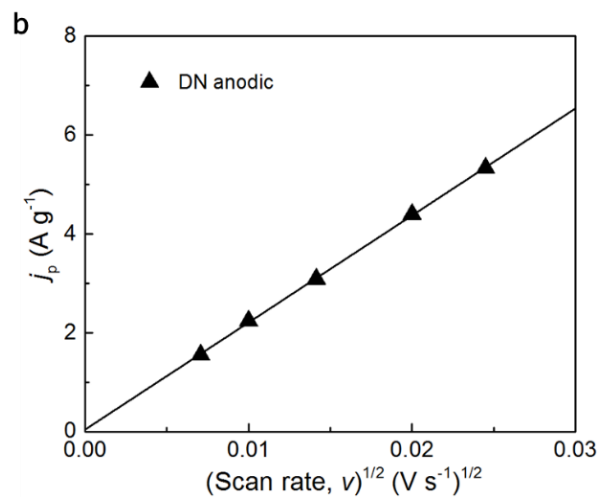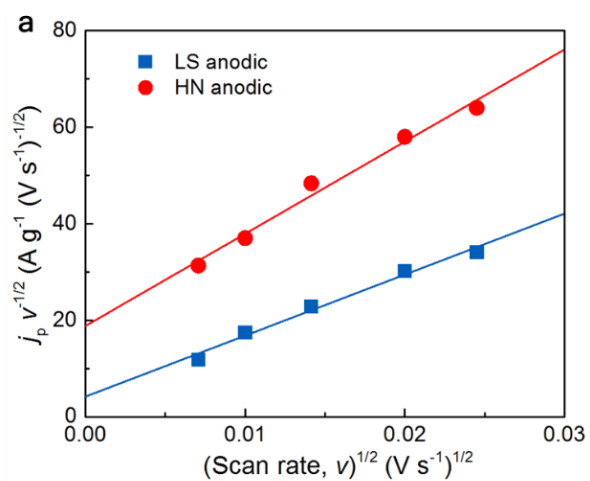
Supplementary Figure 19 | Linear fitting to j_p $v^{-1/2}$ *vs.* $v^{1/2}$ for layered structure (*LS*) and hydrated nanocomposite (*HN*) electrode materials (a) and linear fitting to j_p *vs.* $v^{1/2}$ for dry nanocomposite (*DN*) electrode materials (b).
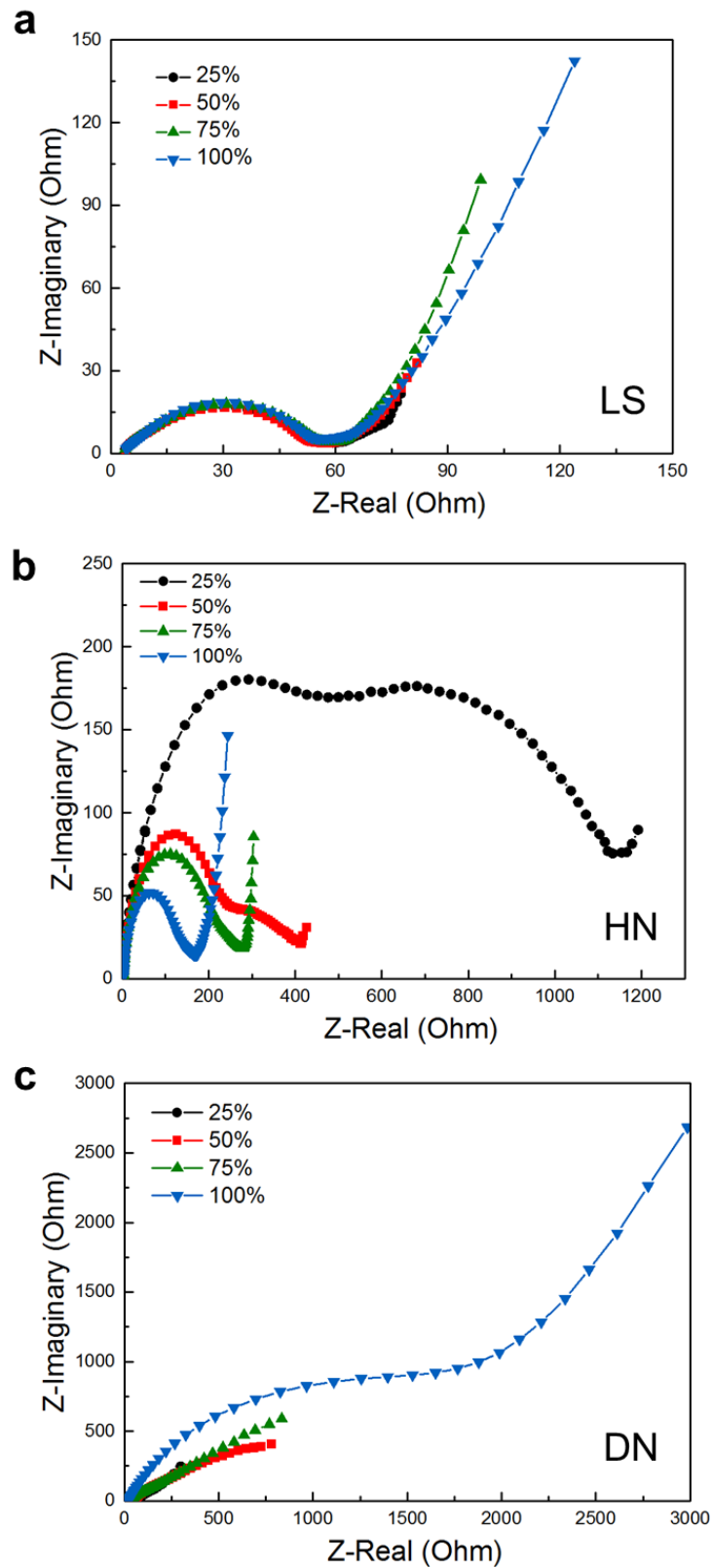
Supplementary Figure 20 | EIS analysis of as-synthesized electrodes measured at different depths of discharge. (a) Layered structure (*LS*), (b) hydrated nanocomposite (*HN*) and (c) dry nanocomposite (*DN*) electrodes.
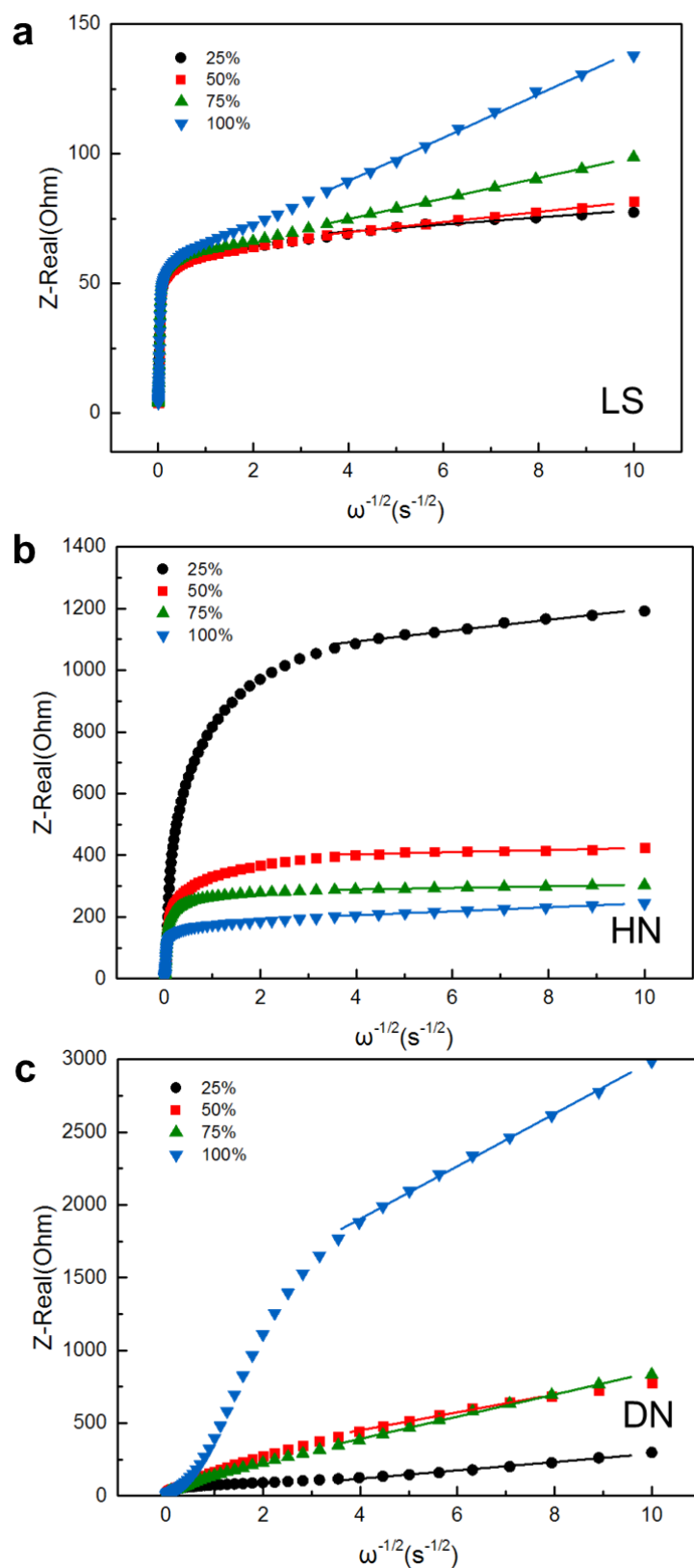
Supplementary Figure 21 | Z' vs. $\omega^{-1/2}$ plots of as-synthesized electrodes in the low frequency region obtained from EIS measurements. (a) Layered structure (*LS*), (b) hydrated nanocomposite (*HN*) and (c) dry nanocomposite (*DN*) electrodes.
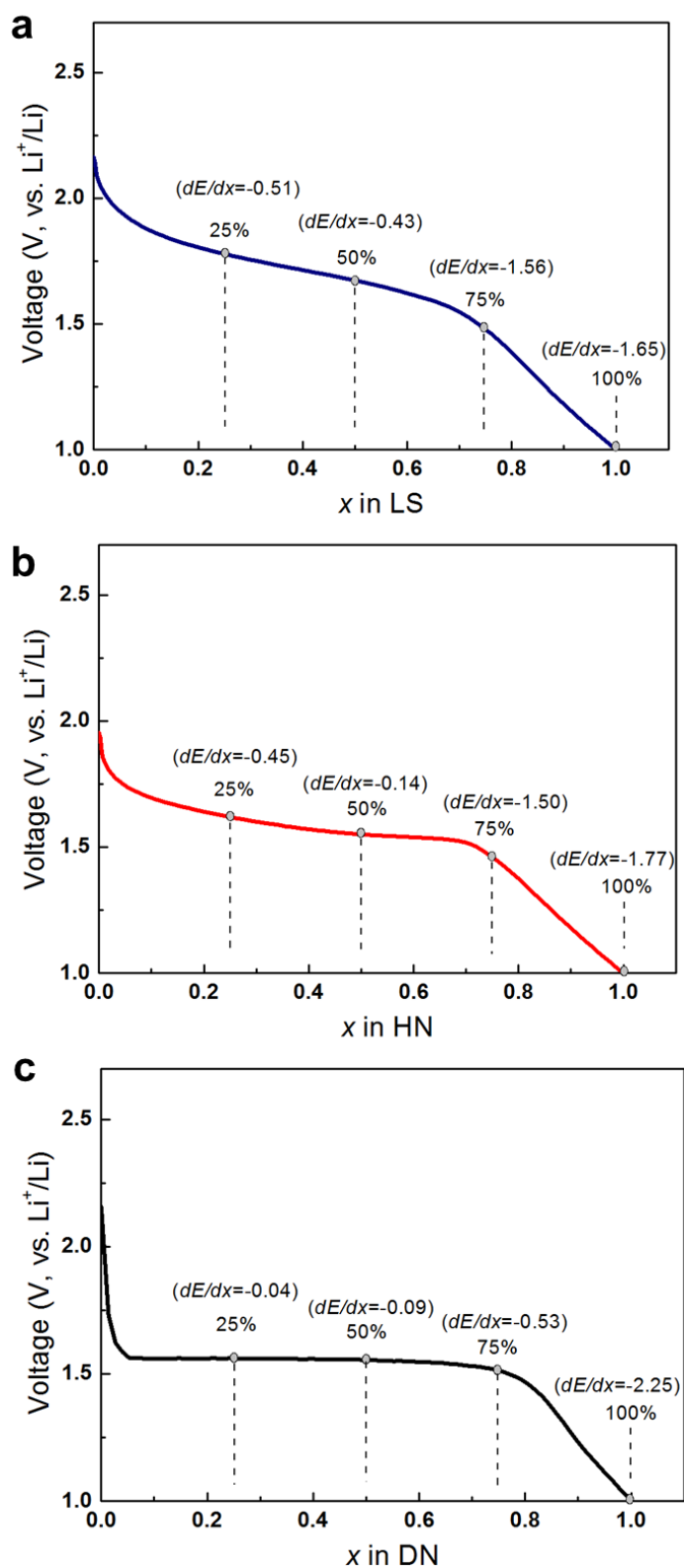
Supplementary Figure 22 | Discharge curves of as-synthesized electrodes at a current density of 50 mA g⁻¹. (a) Layered structure (*LS*), (b) hydrated nanocomposite (*HN*) and (c) dry nanocomposite (*DN*) electrodes.
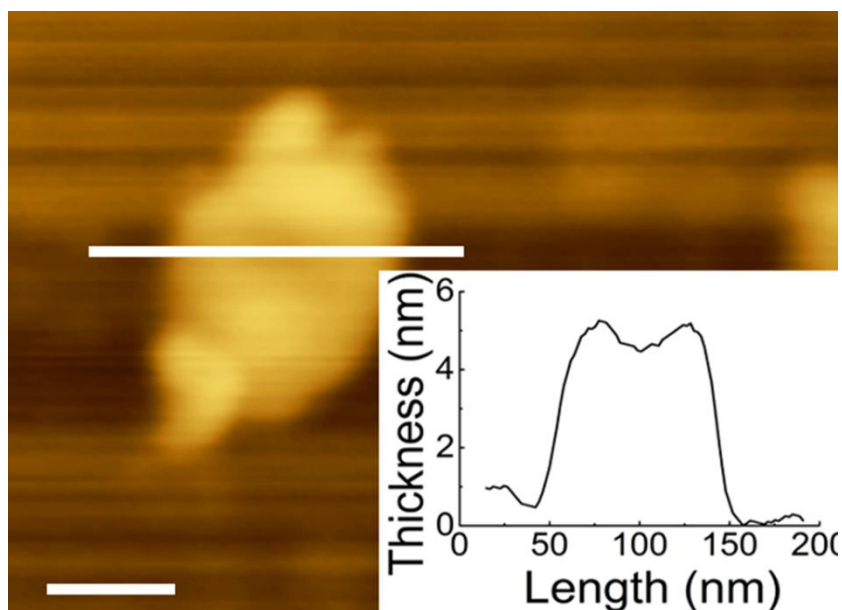
Supplementary Figure 23 | AFM image of hydrated nanocomposite (*HN*). The insert shows its corresponding thickness analysis conducted along the white line. *Scale bar*, 100 nm.
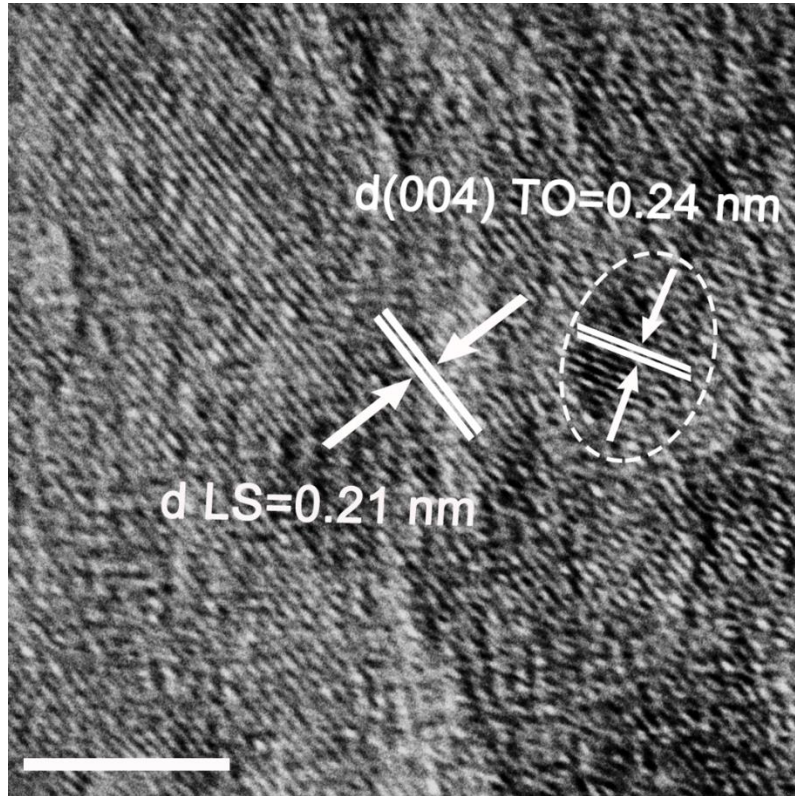
Supplementary Figure 24 | HRTEM image of a hydrated nanocomposite (*HN*) with a spacing of 0.21 nm for layered structure (*LS*) and 0.24 nm for anatase TiO₂. *Scale bar*, 100 nm.
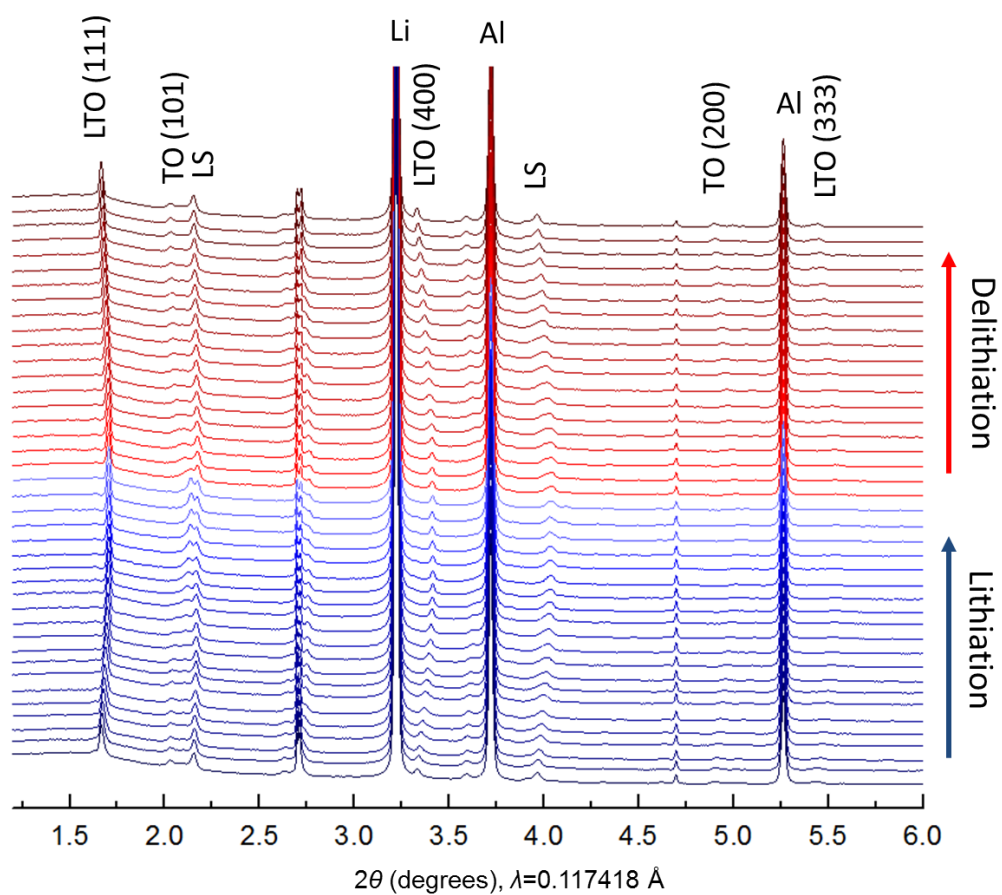
Supplementary Figure 25 | *In situ* synchrotron XRD results during the third cycle of hydrated nanocomposite (*HN*) electrode cycled at 100 mA g⁻¹.
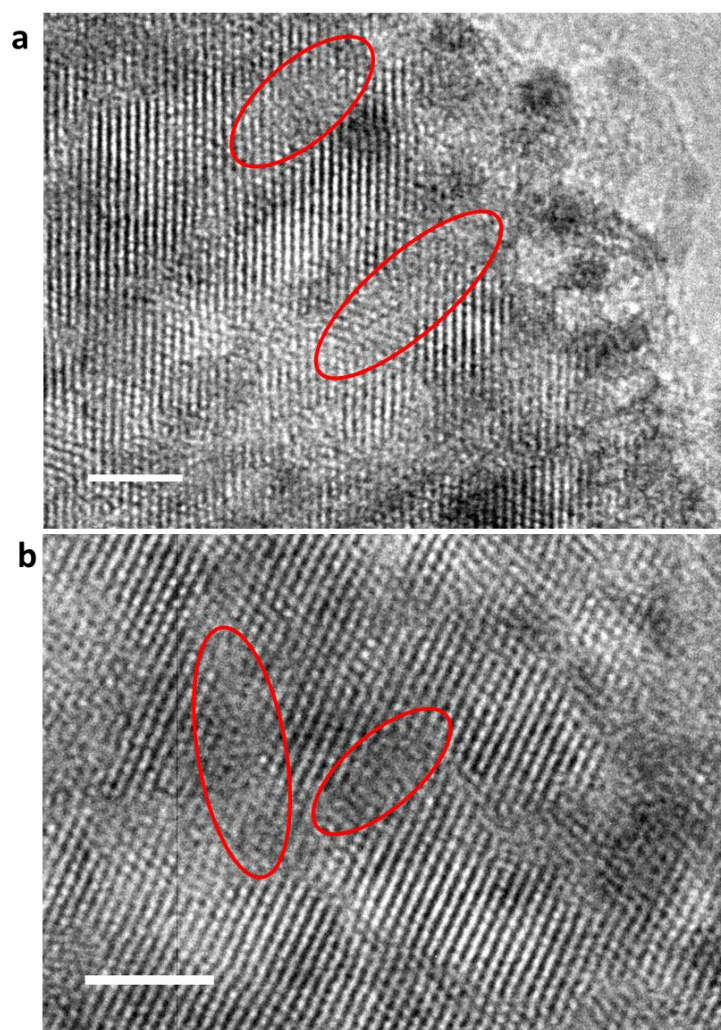
Supplementary Figure 26 | HRTEM images of hydrated nanocomposite (*HN*). The lattice distortion and disorder at the interfaces are illustrated in red circles. *Scale bar*, 5 nm (a, b).
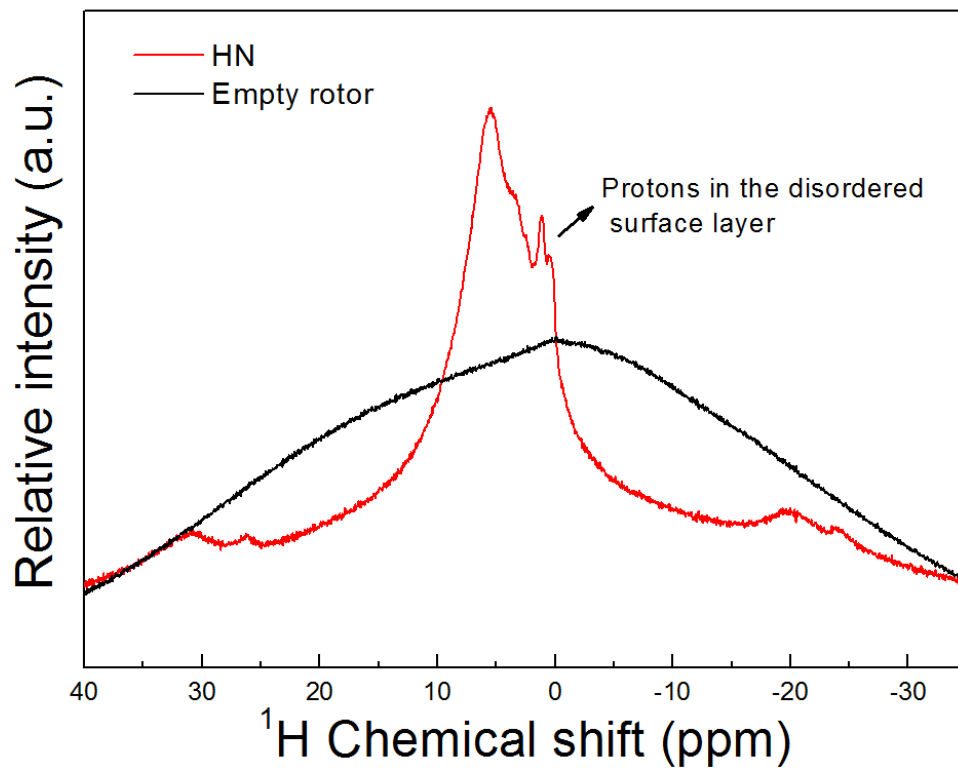
Supplementary Figure 27 | **¹H solid state MAS-NMR spectra of hydrated nanocomposite (*HN*).**
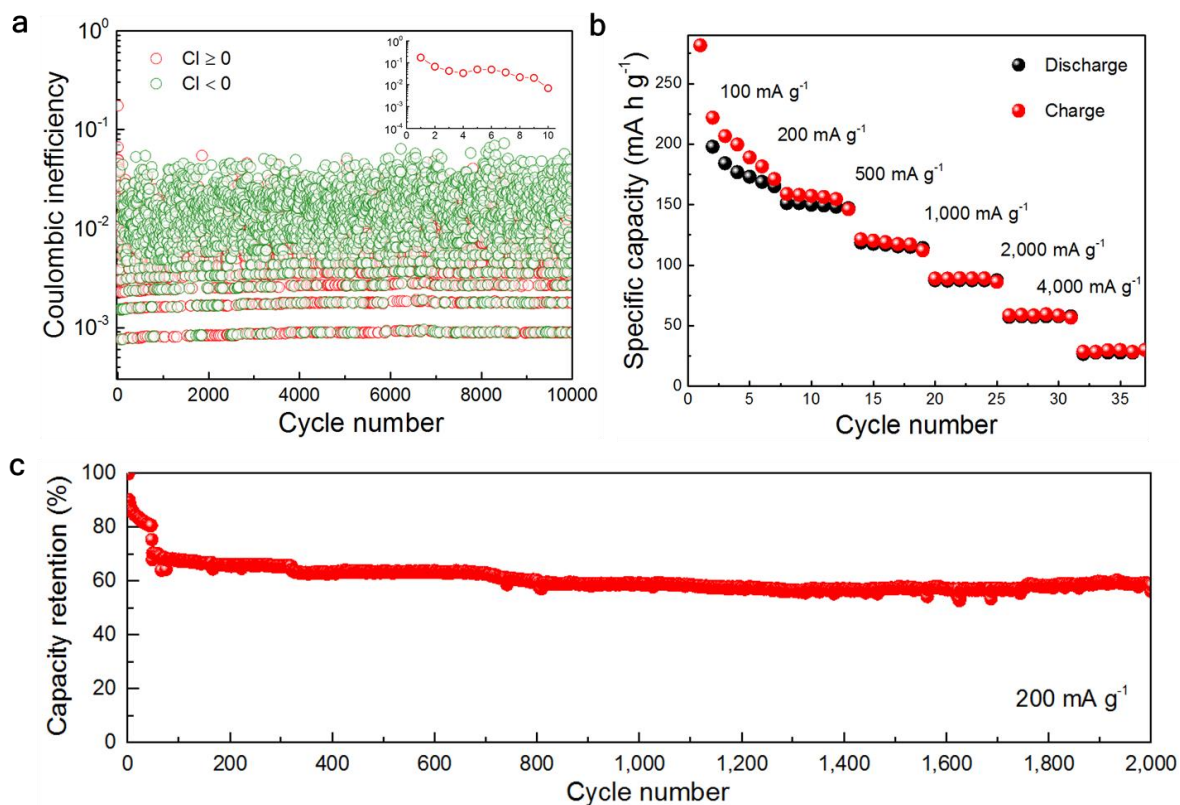
Supplementary Figure 28 | Electrochemical performances of hydrated nanocomposite (*HN*).
(a) Coulombic inefficiency of hydrated nanocomposite (*HN*) at 4,000 mA g^{-1}, the insert magnifies CI for the first 10 cycles. (b) The rate performances and (c) capacity retention at 200 mA g^{-1} for LiFePO$_4$ *vs.* HN full batteries.

Supplementary Table 1 | Comparison of the electrochemical performances of the as-prepared lithium titanate hydrates with previously reported high-rate anode materials on the Li_2O-TiO_2 axis. Their electrode compositions are listed using the mass ratio of active materials: conductive carbon: binder.

Materials	Synthesis temperature (ºC)	Electrode compositions	Loading density (mg cm^{-2})	High rate capacity (mAh g^{-1})	Cycling capacity retention after cycles	References
Lithium titanate hydrates (HN)	260	80:10:10	~1.0	124 (~70C)	86%, 10,000 cycles (~35C)	this work
Lithium titanate hydrates (LS)	190	80:10:10	~1.0	91 (~70C)	76%, 1,000 cycles (~70C)	this work
$Li_4Ti_5O_{12}$ nanowires without carbon coating	500~700	100:0:0	N/A	119 (30C)	80%, 100 cycles (5C)	1
$Li_4Ti_5O_{12}$ nanosheet arrays without carbon coating	550	100:0:0	0.04	78 (200C)	92.5%, 3,000 cycles (50C)	2
Large-pore Mesoporous $Li_4Ti_5O_{12}$ thin film without carbon coating	650	100:0:0	0.05	155 (32C)	95%, 3,000 cycles (64C)	3
$Li_4Ti_5O_{12}$ nanosheets with N-doped carbon coating	600	100:0:0	N/A	131 (100C)	99%, 100 cycles (10C)	4
Self-supported $Li_4Ti_5O_{12}$-C nanotube arrays	550	100:0:0	0.42	80 (100C)	93%, 500 cycles (10C)	5
Porous $Li_4Ti_5O_{12}$ without carbon coating	700~800	85:10:5	0.8~1.0	105 (30C)	98%, 500 cycles (5C)	6
Mesoporous $Li_4Ti_5O_{12}$ hollow spheres without carbon coating	500	70:20:10	N/A	104 (20C)	88%, 300 cycles (5C)	7
Mesoporous $Li_4Ti_5O_{12}$ with carbon coating	700	80:10:10 90:0:10	N/A	115 (10C) 90 (5C)	90%, 500 cycles (10C)	8
Porous $Li_4Ti_5O_{12}$ spheres with N-doped carbon coating	600	80:10:10	N/A	130 (10C)	83%, 2200 cycles (2C)	9
Compact $Li_4Ti_5O_{12}$ spheres with carbon coating	700	80:10:10	1.5	148.6 (10C)	97.3%, 500 cycles (10C)	10
Ti^{3+}-free three-phase $Li_4Ti_5O_{12}/TiO_2$	500	80:10:10	1.0	156 (50C)	80%, 1000 cycles (25C)	11
$Li_4Ti_5O_{12}$ with mesoporous carbon matrix	750	90:2:8	N/A	92.6 (40C)	94.4%, 1,000 cycles (20C)	12
$Li_4Ti_5O_{12}$ micro-spheres/ carbon textiles	550	80:12:8	N/A	119 (60C)	94.7%, 200 cycles (10C)	13
Tailored $Li_4Ti_5O_{12}$/ cathodically induced graphene composite	800	80:10:10	1.3	126 (100C)	74.6%, 500 cycles (25C)	14
Monodisperse $Li_4Ti_5O_{12}$ nanospheres	750	80:10:10	~2.0	108.9 (80C)	92.6%, 500 cycles (10C)	15
Templated spinel $Li_4Ti_5O_{12}$	--	90:5:5	0.8	85 (200C)	--	16
Elongated bending TiO_2(B) nanotube without carbon coating	400	100:0:0	N/A	164 (15C)	~70%, 10,000 cycles (25C)	17
Mesoporous TiO_2(B) microspheres without carbon coating	500	75:15:15	1~2	115 (60C)	90%, 5,000 cycles (10C)	18
Porous TiO_2(B) nanosheets without carbon coating	350	70:20:10	~1	202 (10C)	92.6%, 200 cycles (10C)	19
TiO_2(B) nanosheets on active carbon fabric	350	80:10:10	1.0~1.2	97 (30C)	87%, 2,000 cycles (20C)	20
Gel-like TiO_2-based nanotubes	500	100:0:0	0.3~0.5	133 (30C)	86%, 6,000 cycles (30C)	21
Ti^{3+} self-doped rutile TiO_2 nanorods	N/A	75:15:15	1.0~1.2	93.6 (50C)	98.4%, 1,000 cycles (50C)	22

Supplementary Table 2 | The intensity value for TOF-SIMS profile in Supplementary Figure 7.

Deepness (nm)	H	O	Ti
1.18	8.00	2.00	81.11
1.77	9.00	4.00	79.11
2.36	4.00	4.00	76.10
2.95	7.00	4.00	90.13
3.54	10.00	5.00	87.12
4.13	9.00	5.00	86.12
4.72	7.00	1.00	92.15
5.31	10.00	1.00	96.15
5.9	8.00	8.00	90.14
6.49	12.00	2.00	100.18
7.08	6.00	6.00	101.17
7.67	6.00	1.00	97.17
8.26	11.00	4.00	96.15
8.85	7.00	7.00	84.12
9.44	5.00	3.00	78.10
10.03	10.00	1.00	83.13
10.62	8.00	2.00	91.14

Supplementary Table 3 | The calculated relative ratio of pseudocapacitive and bulk diffusion currents (I_c: I_d) for layered structure (*LS*) and hydrated nanocomposite (*HN*) electrode materials at different sweep rates.

Sweep rate (mV s^{-1})	LS anodic	HN anodic
0.05	2.15	0.72
0.1	3.03	1.02
0.2	4.29	1.44
0.4	6.07	2.03
0.6	7.43	2.49

Supplementary Table 4 | The Li-ion diffusion coefficients of layered structure (*LS*), hydrated nanocomposite (*HN*) and dry nanocomposite (*DN*) electrodes at different depths of discharge marked in Supplementary Fig. 22.

Depth of discharge / Diffusion coefficient	LS cm^2 s^{-1}	HN cm^2 s^{-1}	DN cm^2 s^{-1}
25%	2.10×10^{-8}	2.72×10^{-10}	4.87×10^{-13}
50%	8.34×10^{-9}	2.93×10^{-10}	2.66×10^{-13}
75%	2.46×10^{-8}	1.00×10^{-9}	6.81×10^{-14}
100%	8.21×10^{-9}	1.17×10^{-8}	2.46×10^{-11}

Supplementary Note 1 (Supplementary Figure 4): A main peak at about 3400 cm^{-1} is associated with O–H stretching vibration and most probably as Ti–OH surface group.[23]

Supplementary Note 2 (Supplementary Figure 5): Even at relative low current density of 100 mA g^{-1}, the discharge specific capacity of LTHs-precursor electrodes plummeted from 258.5 mA h g^{-1} to 59.7 mA h g^{-1} for the first 50 cycles, showing an unsatisfactory cycling performance in aprotic electrochemical system.

Supplementary Note 3 (Supplementary Figure 7): It was measured on (100)-oriented silicon wafer showing the distribution of proton together with other elements, as a function of depth from the top surface. H, O and Ti elements exhibited some fluctuation from Supplementary Table 2, implying the step function in the layered structures.

Supplementary Note 4 (Supplementary Figure 11): Before the growth of $Li_4Ti_5O_{12}$-TiO_2 crystallites, LS has a relatively higher surface area of 120 m^2 g^{-1}. With the rising dehydration temperature, the surface area of HN decreased to 103 m^2 g^{-1}. At the end of the dehydration and phase transition progress, DN showed the lowest surface area of 10 m^2 g^{-1} caused by an ever-increasing aggregation or coarsening of nanoparticles.

Supplementary Note 5 (Supplementary Figure 12): The dominated pairs of sharp redox peaks at about 1.73 V and 1.44 V corresponding to the diffusion-controlled process in $Li_4Ti_5O_{12}$ phase, while the pseudocapacitive behavior of LS at around 1.75 V and the diffusion-controlled behavior of TiO_2 at 1.7 V/2.0 V were superimposed upon each other to produce two flat and wide peaks.

Supplementary Note 6 (Supplementary Figure 13): The lithium titanate anode LTO-400 and LTO-500 were also synthesized by heating the LTHs precursor at 400 °C and 500 °C, respectively, and kept the other experimental variables fixed. The electrochemical performances among LS, HN, LTO-400 and LTO-500 materials was illustrated in Supplementary Fig. 13b. LTO-400 can deliver more specific capacity (125 mAh g^{-1}) in the initial cycle compared to LS and HN, however, its capacity drops from 118 mAh g^{-1} to 66 mAh g^{-1} in the first three thousand cycles and then tapers

off to 36 mAh g^{-1} in the following several thousand cycles. Similarly, the capacity of LTO-500 plummets from 148 mAh g^{-1} to 74 mAh g^{-1} in the first three thousand cycles and maintains only 51 mAh g^{-1} after 10,000 cycles. The reason is that Li$_4$Ti$_5$O$_{12}$ and TiO$_2$ with mainly diffusion-controlled redox reaction can usually storage more Li-ions than LS with mainly surface-controlled redox reaction, but the Li-ion diffusion coefficient of Li$_4$Ti$_5$O$_{12}$ and TiO$_2$ is lower than the 2D materials of LS and HN, resulting in the relatively unsatisfactory cycling performances of LTO-400 and LTO-500 electrodes.

Supplementary Note 7 (Supplementary Figure 15): The XPS was conducted to analyze the surface status and composition of LHTS, LS, HN and DN electrodes after 10,000 cycles at 4000 mA g^{-1}. The electrodes were carefully separated from the other components of the coin cell and washed with DMC to remove the electrolyte. All the operations were conducted in a glove box under Argon atmosphere.

In the comparison of C 1s spectrum (Supplementary Fig. 15a), three main peaks at 289.8, 286.5 and 284.8 eV can be assigned to carbon atoms in a three-oxygen environment (CO$_3$-like), one-oxygen environment (CO-like), carbon atom bound only to C or H atoms, respectively. These three carbon species could demonstrate the presence of Li$_2$CO$_3$ and lithium alkyl carbonate (ROCOOLi) well.[24,25] The possible SEI formation mechanisms are as follows: i) intrinsic catalysis by Ti^{4+} species during the discharge process, Ti^{3+} is oxidized to Ti^{4+}, whereby the latter species may have a catalytic influence on the electrolyte decomposition (Ti^{4+} + EC/PC/DMC$\rightarrow$Ti^{3+} + radicals + CO$_2$); ii) electrolyte (EC) reduction from lithiated LTO (2Li$^+$ + EC $\rightarrow$ Li$_2$CO$_3$ / (CH$_2$CH$_2$OLi)$_2$ + C$_2$H$_4$).[26, 27]

In the comparison of F 1s spectrum (Supplementary Fig. 15b), two peaks at 687.1 and 684.6 eV can be assigned to PVDF and LiF, respectively. For DN which is completely water-free, a small amount of the LiF was observed which could be caused by some possibilities as follows: a) the hydrolysis of LiPF$_6$ (LiPF$_6$+H$_2$O$\rightarrow$LiF+POF$_3$+2HF), as water unavoidably exists in a very low concentration (ppm) in the electrolyte; b) LiPF$_6$ salt would decompose by itself during reduction in the charge/discharge cycles (LiPF$_6$$\rightarrow$LiF+PF$_5$); c) salt reaction with products such as Li$_2$CO$_3$, resulting from reaction (PF$_5$+Li$_2$CO$_3$$\rightarrow$2LiF+POF$_3$+CO$_2$, LiPF$_6$+Li$_2CO_3$$\rightarrow$3LiF +POF$_3$+CO$_2$, et al).[28,29] The intensity of LiF peak gradually increased from HN to LS, which implied that more

structural water might be broken and released into the electrolyte during long-term and super-fast cycling process, resulting in slight hydrolysis of $LiPF_6$. This could be the reason of the slight capacity fading of LS and HN. As a contrast, there shows much more LiF at the surface of LTHs electrodes due to the strong peak of LiF. This result demonstrate that the electrodes with more loosely bound water (such as crystallographic water) would be more likely to cause the decomposition of $LiPF_6$, leading to electrochemical performances worsened rapidly in aprotic electrolyte.

Supplementary Note 8 (Supplementary Figure 16, 17): For quite some time, the researchers considered that PF_5, a strong Lewis acid and one of the decomposition products of $LiPF_6$, is the major source of the side reactions in the presence of trace amount of water. According to the analysis about formation mechanism of SEI film above, many recent reports have illustrated that the electrolyte (say, EC/PC/DMC) decomposition by Ti^{4+} species and electrolyte (say, EC) reduction from lithiated LTO are the main side reactions for Ti-based materials during charging/discharging process.[26,27] We have designed the following experiments using LiTFSI as electrolyte salts (1M LiTFSI in EC and DMC (1:1 by volume)) to support the opinion mentioned above. As LiTFSI salt is not sensitive to water, therefore if the side reactions will still happen between the electrode and electrolyte, there could be some else decomposition mechanism resulting in unsatisfactory "Coulombic inefficiency" (CI).[30]

We further tested some electrochemical performances of HN when using different lithium salts (LiTFSI and $LiPF_6$). The CI of HN electrode with LiTFSI electrolyte (hereinafter refer as HN-LiTFSI, Supplementary Fig. 16) is quite similar with that of HN electrode with $LiPF_6$ electrolyte (hereinafter refer as HN-$LiPF_6$), especially for the first 10 cycles, implying that the main decomposition mechanism may not be the hydrolysis of $LiPF_6$ with trace amount of water. Besides, the rate performance as well as cyclability of HN-LiTFSI are also similar with HN-$LiPF_6$. This phenomenon could demonstrate that the SEI formed after several cycles on the surface of HN with LiTFSI electrolyte is as stable as the one formed on the surface of HN with $LiPF_6$ electrolyte, thus both two HN electrodes with different lithium salts could exhibit excellent high-rate capacity and cycling stability. In the same way, we also illustrated electrochemical performances of LS when using LiTFSI as lithium salts (Supplementary Fig. 17). The result and trend are the same as

the condition of HN discussed above.

Supplementary Note 9 (Supplementary Figure 18): The contribution of pseudocapacitity and diffusion-controlled capacity was further revealed by analyzing the cyclic voltammetry data (in Supplementary Figure 18) and can be quantified according to the following Equation (1-2):[31,32]

$$j_p = k_1 v + k_2 v^{1/2} \tag{1}$$

or

$$j_p v^{-1/2} = k_1 v^{1/2} + k_2 \tag{2}$$

where $k_1 v$ represents pseudocapacitive current (I_c) contributed by interfacial storage and bulk faradic pseudocapacitance; $k_2 v^{1/2}$ represents the (bulk) diffusion current (I_d). The coefficients k_1 and k_2 can be determined by linear fitting to $j_p v^{-1/2}$ *vs.* $v^{1/2}$ in Supplementary Fig. 19a. Therefore, it is possible to calculate the relative contribution of I_c and I_d at specific scan rate (v).

Supplementary Note 10 (Supplementary Figure 19): The results of I_c: I_d for LS and HN electrodes are illustrated in Supplementary Table 3. It should be noted that I_c: I_d for LS is relatively high compared to that of HN, even at relatively low sweep rate of 0.05 mV s^{-1}. This result demonstrates that pseudocapacitive feature of LS, which is consistent with the electrochemical mechanism analysis in Figure 4a. For HN, at relatively low scan rate (0.05 mV s^{-1}), the relative ratio of I_c: I_d is 0.72, indicating the mixed pseudocapacitive and diffusion-controlled mechanism of HN. At the sweep rate of 0.1 mV s^{-1}, the pseudocapacitive storage current is approximately equal to the bulk storage current. The capacitive currents might be due to the synergistic effect of the pseudocapacitive feature of LS and nano-size effect of LTO and TO as well as large amount of interfaces among LTO-TO-LS. With a further increase of the sweep rate, the pseudocapacitive current eventually dominates the total current. For DN, the storage current density j_p illustrates a good linear relationship with $v^{1/2}$, implying that DN is totally diffusion controlled (Supplementary Fig. 19b).

Supplementary Note 11 (Supplementary Figure 20-22): The low-frequency Warburg contribution of the impedance response has been used to determine the Li-ion diffusion coefficient (D_{Li}) at various state of discharge in the electrodes (Supplementary Fig. 22). The expression for

D_{Li} can be written as:[33,34,35]

$$D_{Li} = \frac{1}{2}\left[\left(\frac{V_m}{FA\sigma_w}\right)\frac{dE}{dx}\right]^2 \qquad (3)$$

where V_m is the molar volume (we defined V_m for all three materials as 45.73 cm^3 mol^{-1} (Li$_4$Ti$_5$O$_{12}$) for simplification), F is the Faraday constant, A is the total contact area between the electrolyte and the electrode, and σ_w is the Warburg coefficient which was obtained from the Warburg region of impedance response. The σ_w values at different discharge depths (different potentials) can be obtained from the slope of lines in Z' *vs.* $\omega^{-1/2}$ plots (ω is the angular frequency) for the Warburg region. As shown in (Supplementary Fig. 21), the Z' *vs.* $\omega^{-1/2}$ plot for the low frequency Warburg region can be summarized as:

$$Z' = R + \sigma_w\omega^{-1/2} \qquad (4)$$

The *dE/dx* obtained from discharge curve illustrates that the slopes of the discharge curve at 25%, 50%, 75% and 100% respectively (Supplementary Fig. 22). Each sample was activated for 10 cycles between 1.0-2.5V at 50 mA g^{-1} before test and stopped according to the percentage of the total discharge capacity (as shown in Supplementary Fig. 22). The EIS measurement was conducted right after the cell was stopped, and then it was charged/discharged for 2 complete cycles between 1.0-2.5V at 50 mA g^{-1} before the next measurement.

The reason why the Li-ion diffusion coefficients at 25%, 50% and 75% are lower than 100% is that 25%-75% of the HN and DN electrodes are associated the two-phase region, in which the total Li-ion insertion process is limited by Li-ion diffusion across the interface.[36] Therefore the Li-ion diffusion within the two-phase region is much lower than the Li-ion diffusion within the single-phase regions. However, there is a little change of D_{Li} for LS (8.21×10^{-9}-2.46×10^{-8} cm^2 s^{-1}), which might due to the surface-controlled feature of LS (here "surface" is taken to mean in the broad sense, that may include spacing between two adjacent LS monolayers).

Supplementary Note 12 (Supplementary Figure 25): Note that the LTO in our system reveal much larger lattice changes and we expected that this phenomenon might be ascribed to the size effect[37] and the existence of abundant lattice distortion and disorder[38] in HN composite.

Supplementary Note 13 (Supplementary Figure 27): From the result of blank rotor, no sharp

signals appear at low chemical shift. The large line width in the ^{1}H NMR spectra can be attributed to both dipole-dipole interactions and an intrinsic chemical shift spread, as proton bridging sites are located on different crystallographic planes in the structure. Two small sharpness ^{1}H NMR resonances at chemical shifts of 1.14 ppm and 0.56 ppm are associated with isolated OH groups without hydrogen bonds[39] and protons located in the disordered surface layer among $Li_4Ti_5O_{12}$-TiO_2-LS[40], respectively.

Supplementary Note 14 (Supplementary Figure 28): Herein, we will evaluate the possibility of in full batteries of HN material by using the concept of "Coulombic inefficiency".[30] In half cells, as the "live Li-ion" in pure lithium counter electrode is infinite compared to the working electrode, the electrochemical performance of working electrode is not affected by the CE or CI at all. However, when it comes to full cells, almost all the "live Li-ion" are from the cathode (i.e. $LiFePO_4$, $LiCoO_2$, *etc.*), if the CE (half cell) of the anode cannot be higher than 99.5% in less than 10 cycles, one solution is to use the slightly excess cathode as the supplement of "live Li-ion". However, if the CE$_{stabilized}$ is lower than 99.9% after 10 or more cycles, the "live Li-ion" would be consumed rapidly even if the cathode is several hundreds percent excess to the anode. In this situation, it is impossible to get a satisfactory cycling performance in full cells.

Supplementary Figure 28a illustrates calculated CI for HN electrode at 4,000 mA g^{-1}. The CI value for the first cycle is 10^{-1}, and then it dropped to $<10^{-2}$ after 10th cycle, followed by fluctuating values distributed between 10^{-2} and 10^{-4} for the following 10,000 cycles. We note that there are more number of negative (green) CIs than positive (red) CIs, which means if a running-window average is done, the average CE actually exceeds 1 by a little. This may be explained by the reversible shuttling of soluble redox mediators in the electrolyte.[41] This result illustrated HN electrode could possess excellent SEI stability and highly reversible Li-ion insertion/extraction properties, because if the SEI were to fall off / regrow repeatedly with cycling, the average CE should be less than 1 (average CI should be positive). To further verify this, we assembled $LiFePO_4$ cathode *vs.* HN anode in full batteries using the same electrolyte in half cells and test their performances between 1.2 and 2.4 V. The full battery delivered specific capacity of 168, 149, 117, 89, 58 and 28 mA h g^{-1} in the 100, 200, 500, 1,000, 2,000 and 4,000 mA g^{-1} (Supplementary Fig. 28b). For the cycling performance at 200 mA g^{-1} in Supplementary Fig. 28c, 30% of the initial

capacity is lost in the first 50 cycles due to SEI growth and some side reactions for the electrodes. However, the cyclability tends to be quite stable for the next 2,000 cycles with only 10% of the initial capacity lost, indicating that HN is a very promising material as a LIB anode for the real-life energy storage application. It is true that the output voltage of the LiFePO$_4$ *vs.* HN full battery is somewhat low due to the relatively high potential (*vs.* Li) of HN compared with graphite anode. However, the advantages of improved safety over graphite as well as outstanding high-rate and long-cycling performances for lithium titanate hydrates are still obvious in some applications like electric buses, electric vans, smart grids, large-scale storage grids, *et al*.

Supplementary Note 15 (Supplementary Table 1): It is noted that for some diffusion-controlled materials (like LiFePO$_4$), the ionic transport through the electrode and electrolyte is rate limiting when charged/discharged at high current density.[42,43] Therefore, if one electrode is thin or with less mass loading (say, less than 0.5 mg cm^{-2}), it could exhibit better high-rate performance than the thicker one or with higher mass loading. As a result, it is recommended to deal with the comparison above correctly by considering the loading density of each electrode.

Supplementary References:

1 Shen, L. F., Uchaker, E., Zhang, X. G. & Cao, G. Z. Hydrogenated $Li_4Ti_5O_{12}$ Nanowire Arrays for High Rate Lithium Ion Batteries. *Adv. Mater.* **24**, 6502-6506 (2012).

2 Chen, S. *et al.* Self-Supported $Li_4Ti_5O_{12}$ Nanosheet Arrays for Lithium Ion Batteries with Excellent Rate Capability and Ultralong Cycle Life. *Energy Environ. Sci.* **7**, 1924-1930 (2014).

3 Haetge, J. *et al.* Ordered Large-Pore Mesoporous $Li_4Ti_5O_{12}$ Spinel Thin Film Electrodes with Nanocrystalline Framework for High Rate Rechargeable Lithium Batteries: Relationships Among Charge Storage, Electrical Conductivity, and Nanoscale Structure. *Chem. Mater.* **23**, 4384-4393 (2011).

4 Li, N. *et al.* A Self-Standing and Flexible Electrode of $Li_4Ti_5O_{12}$ Nanosheets with a N-Doped Carbon Coating for High Rate Lithium Ion Batteries. *Adv. Funct. Mater.* **23**, 5429-5435 (2013).

5 Liu, J. *et al.* Self-Supported $Li_4Ti_5O_{12}$-C Nanotube Arrays as High-Rate and Long-Life Anode Materials for Flexible Li-Ion Batteries. *Nano Lett.* **14**, 2597-2603 (2014).

6 Hasegawa, G. *et al.* Hierarchically Porous $Li_4Ti_5O_{12}$ Anode Materials for Li-and Na-Ion Batteries: Effects of Nanoarchitectural Design and Temperature Dependence of the Rate Capability. *Adv. Energy Mater.* **5**, 1400730 (2015).

7 Yu, L., Wu, H. B. & Lou, X. W. Mesoporous $Li_4Ti_5O_{12}$ Hollow Spheres with Enhanced Lithium Storage Capability. *Adv. Mater.* **25**, 2296-2300 (2013).

8 Kang, E. *et al.* Highly Improved Rate Capability for a Lithium-Ion Battery Nano-$Li_4Ti_5O_{12}$ Negative Electrode via Carbon-Coated Mesoporous Uniform Pores with a Simple Self-Assembly Method. *Adv. Funct. Mater.* **21**, 4349-4357 (2011).

9 Zhao, L. *et al.* Porous $Li_4Ti_5O_{12}$ Coated with N-Doped Carbon From Ionic Liquids for Li-Ion Batteries. *Adv. Mater.* **23**, 1385-1388 (2011).

10 Wang, C. *et al.* Combining Fast Li-Ion Battery Cycling with Large Volumetric Energy Density: Grain Boundary Induced High Electronic and Ionic Conductivity in $Li_4Ti_5O_{12}$ Spheres of Densely Packed Nanocrystallites. *Chem. Mater.* **27**, 5647-5656 (2015).

11 Wang, S. *et al.* Ti^{3+}-Free Three-Phase $Li_4Ti_5O_{12}/TiO_2$ for High-Rate Lithium Ion Batteries: Capacity and Conductivity Enhancement by Phase Boundaries. *Nano Energy* **32**, 294-301 (2017).

12 Shen, L. *et al.* $Li_4Ti_5O_{12}$ Nanoparticles Embedded in a Mesoporous Carbon Matrix as a Superior Anode Material for High Rate Lithium Ion Batteries. *Adv. Energy Mater.* **2**, 691-698 (2012).

13 Shen, L. *et al.* Advanced Energy-Storage Architectures Composed of Spinel Lithium Metal Oxide Nanocrystal On Carbon Textiles. *Adv. Energy Mater.* **3**, 1484-1489 (2013).

14 Yang, Y. *et al.* Lithium Titanate Tailored by Cathodically Induced Graphene for an Ultrafast Lithium Ion Battery. *Adv. Funct. Mater.* **24**, 4349-4356 (2014).

15 Wang, C. *et al.* A Robust Strategy for Crafting Monodisperse $Li_4Ti_5O_{12}$ Nanospheres as Superior Rate Anode for Lithium Ion Batteries. *Nano Energy* **21**, 133-144 (2016).

16   Singh, D. P., Mulder, F. M. & Wagemaker, M. Templated Spinel $Li_4Ti_5O_{12}$ Li-Ion Battery Electrodes Combining High Rates with High Energy Density. *Electrochem. Commun.* **35**, 124-127 (2013).

17   Tang, Y. *et al.* Mechanical Force-Driven Growth of Elongated Bending TiO_2-Based Nanotubular Materials for Ultrafast Rechargeable Lithium Ion Batteries. *Adv. Mater.* **26**, 6111-6118 (2014).

18   Liu, H. S. *et al.* Mesoporous TiO_2-B Microspheres with Superior Rate Performance for Lithium Ion Batteries. *Adv. Mater.* **23**, 3450-3454 (2011).

19   Liu, S. H. *et al.* Nanosheet-Constructed Porous TiO_2-B for Advanced Lithium Ion Batteries. *Adv. Mater.* **24**, 3201-3204 (2012).

20   Liu, S. H. *et al.* A Flexible $TiO_2(B)$-Based Battery Electrode with Superior Power Rate and Ultralong Cycle Life. *Adv. Mater.* **25**, 3462-3467 (2013).

21   Tang, Y. *et al.* Unravelling the Correlation Between the Aspect Ratio of Nanotubular Structures and their Electrochemical Performance to Achieve High-Rate and Long-Life Lithium-Ion Batteries. *Angew. Chem. Int. Ed.* **53**, 13488-13492 (2014).

22   Chen, J. *et al.* Ti^{3+} Self-Doped Dark Rutile TiO_2 Ultrafine Nanorods with Durable High-Rate Capability for Lithium-Ion Batteries. *Adv. Funct. Mater.* **25**, 6793-6801 (2015).

23   Suzuki, Y., Pavasupree, S., Yoshikawa, S. & Kawahata, R. Natural Rutile-Derived Titanate Nanofibers Prepared by Direct Hydrothermal Processing. *J. Mater. Res.* **20**, 1063-1070 (2005).

24   Leroy, S. *et al.* Influence of the Lithium Salt Nature over the Surface Film Formation on a Graphite Electrode in Li-Ion Batteries: An XPS Study. *Appl. Surf. Sci.* **253**, 4895-4905 (2007).

25   Dedryvere, R. *et al.* Characterization of Lithium Alkyl Carbonates by X-Ray Photoelectron Spectroscopy: Experimental and Theoretical Study. *J. Phys. Chem. B* **109**, 15868-15875 (2005).

26   He, Y. *et al.* Gassing in $Li_4Ti_5O_{12}$-Based Batteries and its Remedy. *Sci. Rep.* **2**, 1-9 (2012).

27   Imhof, R. In Situ Investigation of the Electrochemical Reduction of Carbonate Electrolyte Solutions at Graphite Electrodes. *J. Electrochem. Soc.* **145** 1081-1087 (1998).

28   Dedryvere, R. *et al.* Surface Film Formation on Electrodes in a $LiCoO_2$/Graphite Cell: A Step by Step XPS Study. *J. Power Sources* **174**, 462-468 (2007).

29   Wen, L. *et al.* Dual Functions of Carbon in $Li_4Ti_5O_{12}$/C Microspheres. *J. Electrochem. Soc.* **162**, A3038-A3044 (2014).

30   Yang, J., Sa, L., Akihiro, K. & Al., E. Self-Healing SEI Enables Full-Cell Cycling of a Silicon-Majority Anode with a Coulombic Efficiency Exceeding 99.9%. *Energy Environ. Sci.* **10**, 580-592 (2017).

31   Augustyn, V., Simon, P. & Dunn, B. Pseudocapacitive Oxide Materials for High-Rate Electrochemical Energy Storage. *Energy Environ. Sci.* **7**, 1597-1614 (2014).

32   Yin, H. *et al.* Influence of Morphologies and Pseudocapacitive Contributions for Charge Storage in V_2O_5 Micro/Nano-Structures. *Electrochim. Acta* **111**, 762-770 (2013).

33 Zaghib, K., Simoneau, M., Armand, M. & Gauthier, M. Electrochemical Study of $Li_4Ti_5O_{12}$ as Negative Electrode for Li-Ion Polymer Rechargeable Batteries. *J. Power Sources* **81–82**, 300-305 (1999).

34 Ho, C., Raistrick, I. D. & Huggins, R. A. Application of A-C Techniques to the Study of Lithium Diffusion in Tungsten Trioxide Thin Films. *J. Electrochem. Soc.* **127**, 343-350 (1980).

35 Zhang, D., Popov, B. N. & White, R. E. Electrochemical Investigation of $CrO_{2.65}$ Doped $LiMn_2O_4$ as a Cathode Material for Lithium-Ion Batteries. *J. Power Sources* **76**, 81-90 (1998).

36 Wang, Y. *et al.* Synthesis and Electrochemical Performance of Nano-Sized $Li_4Ti_5O_{12}$ with Double Surface Modification of Ti(iii) and Carbon. *J. Mater. Chem.* **19**, 6789-6795 (2009).

37 Yu, X. *et al.* A Size-Dependent Sodium Storage Mechanism in $Li_4Ti_5O_{12}$ Investigated by a Novel Characterization Technique Combining *in Situ* X-Ray Diffraction and Chemical Sodiation. *Nano Lett.* **13**, 4721-4727 (2013).

38 Lu, X. *et al.* New Insight into the Atomic-Scale Bulk and Surface Structure Evolution of $Li_4Ti_5O_{12}$ Anode. *J. Am. Chem. Soc.* **137**, 1581-1586 (2015).

39 Takagaki, A. *et al.* Titanium Niobate and Titanium Tantalate Nanosheets as Strong Solid Acid Catalysts. *J. Phys. Chem. B* **108**, 11549-11555 (2004).

40 Xia, T. *et al.* Hydrogenated Surface Disorder Enhances Lithium Ion Battery Performance. *Nano Energy* **2**, 826-835 (2013).

41 Li, S. *et al.* High-Rate Aluminium Yolk-Shell Nanoparticle Anode for Li-Ion Battery with Long Cycle Life and Ultrahigh Capacity. *Nat. Commun.* **6**, 7872 (2015).

42 Fongy, C. *et al.* Electronic and Ionic Wirings Versus the Insertion Reaction Contributions to the Polarization in $LiFePO_4$ Composite Electrodes. *J. Electrochem. Soc.* **157**, A1347-A1353 (2010).

43 Zhang, X., Verhallen, T. W., Labohm, F. & Wagemaker, M. Direct Observation of Li-Ion Transport in Electrodes Under Nonequilibrium Conditions Using Neutron Depth Profiling. *Adv. Energy Mater.* **5**, 1500498 (2015).